NAVAL POSTGRADUATE SCHOOL

MONTEREY, CALIFORNIA

THESIS

DESIGN AND ANALYSIS OF AN EXPERIMENTAL SETUP FOR DETERMINING THE BURST STRENGTH AND MATERIAL PROPERTIES OF HOLLOW CYLINDERS

by

Timothy D. Ponshock

December 2015

Thesis Advisor: Young W. Kwon
Co-Advisor: John D. Molitoris

Approved for public release; distribution is unlimited

THIS PAGE INTENTIONALLY LEFT BLANK

REPORT DOCUMENTATION PAGE

Form Approved OMB No. 0704–0188

Public reporting burden for this collection of information is estimated to average 1 hour per response, including the time for reviewing instruction, searching existing data sources, gathering and maintaining the data needed, and completing and reviewing the collection of information. Send comments regarding this burden estimate or any other aspect of this collection of information, including suggestions for reducing this burden, to Washington headquarters Services, Directorate for Information Operations and Reports, 1215 Jefferson Davis Highway, Suite 1204, Arlington, VA 22202-4302, and to the Office of Management and Budget, Paperwork Reduction Project (0704-0188) Washington, DC 20503.

1. AGENCY USE ONLY *(Leave blank)*	2. REPORT DATE December 2015	3. REPORT TYPE AND DATES COVERED Master's Thesis

4. TITLE AND SUBTITLE DESIGN AND ANALYSIS OF AN EXPERIMENTAL SETUP FOR DETERMINING THE BURST STRENGTH AND MATERIAL PROPERTIES OF HOLLOW CYLINDERS	5. FUNDING NUMBERS
6. AUTHOR(S) Timothy D. Ponshock	

7. PERFORMING ORGANIZATION NAME(S) AND ADDRESS(ES) Naval Postgraduate School Monterey, CA 93943-5000	8. PERFORMING ORGANIZATION REPORT NUMBER

9. SPONSORING /MONITORING AGENCY NAME(S) AND ADDRESS(ES) Lawrence Livermore National Laboratory	10. SPONSORING/MONITORING AGENCY REPORT NUMBER

11. SUPPLEMENTARY NOTES The views expressed in this thesis are those of the author and do not reflect the official policy or position of the Department of Defense or the U.S. Government. IRB Protocol number ____N/A____.

12a. DISTRIBUTION / AVAILABILITY STATEMENT Approved for public release; distribution is unlimited	12b. DISTRIBUTION CODE

13. ABSTRACT (maximum 200 words)

A mechanical device and associated testing procedure were developed to apply internal pressure to open-ended cylinders for determination of various properties, including burst pressure, elastic modulus, and Poisson's ratio. ANSYS finite element analysis software was used to model the operation of the device with aluminum cylinders. Analytic equations for thin and thick cylinders were used to validate the computer model results. Initial mechanical testing was performed with aluminum cylinders to verify results against the finite element model. Glass and carbon fiber composite cylinders were fabricated and tested to failure with the device and the aforementioned properties were found. Finally, carbon fiber composite tensile specimens of the dog-bone shape were tested to failure to compare material properties with those found from the cylinder tests. The test device and methods developed in this research support Lawrence Livermore National Laboratory and the Defense Threat Reduction Agency in the development of the Agent Defeat Penetrator, a next-generation agent defeat weapon.

14. SUBJECT TERMS carbon fiber composite, glass fiber composite, pressure testing, composite cylinder	15. NUMBER OF PAGES 101
	16. PRICE CODE

17. SECURITY CLASSIFICATION OF REPORT Unclassified	18. SECURITY CLASSIFICATION OF THIS PAGE Unclassified	19. SECURITY CLASSIFICATION OF ABSTRACT Unclassified	20. LIMITATION OF ABSTRACT UU

NSN 7540–01-280-5500

Standard Form 298 (Rev. 2–89)
 Prescribed by ANSI Std. 239–18

THIS PAGE INTENTIONALLY LEFT BLANK

**DESIGN AND ANALYSIS OF AN EXPERIMENTAL SETUP FOR
DETERMINING THE BURST STRENGTH AND MATERIAL PROPERTIES OF
HOLLOW CYLINDERS**

Timothy D. Ponshock
Lieutenant, United States Navy
B.S., University of Wisconsin, 2008

Submitted in partial fulfillment of the
requirements for the degree of

MASTER OF SCIENCE IN MECHANICAL ENGINEERING

from the

**NAVAL POSTGRADUATE SCHOOL
December 2015**

Author: Timothy D. Ponshock

Approved by: Young W. Kwon
                   Thesis Advisor

                   John D. Molitoris
                   Co-Advisor

                   Garth V. Hobson
                   Chair, Department of Mechanical and Aerospace Engineering

THIS PAGE INTENTIONALLY LEFT BLANK

ABSTRACT

A mechanical device and associated testing procedure were developed to apply internal pressure to open-ended cylinders for determination of various properties, including burst pressure, elastic modulus, and Poisson's ratio. ANSYS finite element analysis software was used to model the operation of the device with aluminum cylinders. Analytic equations for thin and thick cylinders were used to validate the computer model results. Initial mechanical testing was performed with aluminum cylinders to verify results against the finite element model. Glass and carbon fiber composite cylinders were fabricated and tested to failure with the device, and the aforementioned properties were found. Finally, carbon fiber composite tensile specimens of the dog-bone shape were tested to failure to compare material properties with those found from the cylinder tests. The test device and methods developed in this research support Lawrence Livermore National Laboratory and the Defense Threat Reduction Agency in the development of the Agent Defeat Penetrator, a next-generation agent defeat weapon.

THIS PAGE INTENTIONALLY LEFT BLANK

TABLE OF CONTENTS

LIST OF FIGURES

LIST OF TABLES

THIS PAGE INTENTIONALLY LEFT BLANK

LIST OF ACRONYMS AND ABBREVIATIONS

ADP	Agent Defeat Penetrator
ADW	Agent Defeat Weapon
AGM	air-to-ground missile
BLU	bomb live unit
CBU	cluster bomb unit
CFC	carbon fiber composite
DTRA	Defense Threat Reduction Agency
FEA	finite element analysis
GFC	glass fiber composite
EMC	Energetic Materials Center
LLNL	Lawrence Livermore National Laboratory
WMD	weapons of mass destruction

THIS PAGE INTENTIONALLY LEFT BLANK

ACKNOWLEDGMENTS

THIS PAGE INTENTIONALLY LEFT BLANK

I.   INTRODUCTION

A.   MOTIVATION

The U.S. Defense Threat Reduction Agency (DTRA) was created with two primary purposes: to support combatant commanders in their response to threats related to weapons of mass destruction and to foster research and development as ways and means of countering the WMD threat around the world [1]. Typical high explosive weapons are incapable of producing the extremely high and sustained temperatures required to destroy chemical and biological weapons, so specialized Agent Defeat Weapons (ADW) were developed to reliably destroy such weapons while minimizing the risk of releasing the agent to the environment [2]. Current weapons include the BLU-118/B Thermobaric Weapon, Bomb Live Unit (BLU) -119/B Crash Prompt Agent Defeat Weapon, Cluster Bomb Unit (CBU)-107 Passive Attack Weapon, and High Temperature Incendiary J-1000 [2]. The ADW systems typically consist of a high-temperature incendiary payload on a standard weapon body, such as the Guided Bomb Unit (GBU)-15, GBU-24, GBU-27, GBU-28, GBU-31, or Air-to-Ground Missile (AGM)-130 [2].

The Energetic Materials Center (EMC) at Lawrence Livermore National Laboratory (LLNL) is conducting research and development with DTRA in support of a future ADW known as the Agent Defeat Penetrator (ADP). The ADP concept is shown in Figure 1 and consists of a BLU-109 for hard target penetration and a proprietary thermal filler material developed by LLNL and DTRA.

Figure 1.   Agent Defeat Penetrator Concept, from [3].

The LLNL Agent Defeat Program under Dr. John Molitoris is developing a weaponized payload for the ADP based on cast curable cobalt thermite. This fill is known as CTP-W. The research and development necessary for this agent defeat payload relies heavily on the use of carbon fiber composite (CFC) cases. These CFC cases need to have sufficient strength for compression of the thermite and long confinement times prior to case release. In principle, the strength of the CFC case used for testing should be comparable to steel. In practice, the CFC test cases need to be as strong as possible and have well understood properties. CFC is used for ADP payload testing and development as upon explosive initiation and dispersion there are no high velocity metal fragments created that would damage diagnostic equipment. As a result, the highest fidelity data can be taken by utilizing CFC cases in the dynamic test phase. A typical CFC test cylinder prepared for dynamic testing is shown in Figure 2.

Figure 2.   Carbon Fiber Composite Case Prior to Testing at Lawrence
Livermore National Laboratory Energetic Materials Center, from [3].

Another benefit of CFC cases is the possibility for use in future ADW cases. CFC allows for higher-strength-to-weight ratios as well as alteration of the case properties by small adjustments in the fabrication process such as epoxy formulation or filament winding angle. This could result in a lighter weapon with a case designed for a specified containment time during the fabrication process.

B.   OBJECTIVE

This research strongly supports LLNL/DTRA research on next and future generation weapons for agent defeat, specifically development of the ADP. The primary objective was the development a purely mechanical device capable of testing hollow cylinders to failure without modification to the cylinder. Data recorded during the tests will allow for directly determining the elastic modulus, Poisson's ratio, and burst pressure of the cylinder. Ultimately, this test device will be used to determine the material properties used in the composite cases used for explosive testing by LLNL as well as validation of finite element models of the composite cases.

C.   EXPERIMENTAL OVERVIEW

Six 3.172 mm (0.125 in) thick aluminum, two 6.35 mm (0.25 in) thick aluminum, three glass fiber composite (GFC), and four CFC cylinders were prepared for testing with the test device fabricated for this project. The thick aluminum and two thin aluminum cylinders were machined on a lathe to the proper dimension and were analyzed separately from the remaining aluminum cylinders due to changes in material properties from the machining process. Additionally, three CFC tensile specimens were fabricated for comparison with the results from the CFC cylinders.

All composite cylinders were fabricated by hand by wrapping a strip of composite mesh around a mold to achieve a nominal thickness of 3.172 mm (0.125 in). Several strain gages were attached to the midline of each cylinder to measure hoop and axial strains during the test. A single 90-degree strain gage rosette was attached to each CFC tensile specimen to collect longitudinal and transverse strain data.

All tests were performed at a quasi-static extension rate of 2 mm/min to failure or until the test device reached its limit, whichever occurred first. The data from the aluminum cylinders was used to determine the friction coefficient of the test device. With known friction, the results from the composite cylinder tests were used to determine the burst pressure of all cylinders and the unknown material properties of the composite cylinders such as elastic modulus and Poisson's ratio. The data from the CFC tensile tests was used to validate the capability of the test device to allow for accurate determination of the unknown material properties previously mentioned.

D.   PRIOR RESEARCH

A large body of prior work has been completed on both the analytic and experimental analysis of composite pipes and pressure vessels [4-8]. Research conducted by Onder et al. [4] and Xia et al. [5] determined an elastic solution for the burst pressure of thick-walled composite pressure vessels with an internal pressure. Xing et al. [6] examined the effects of various filament-winding angles to optimize composite filament-wound pressure vessel properties and found an optimum winding angle of greater than 55 degrees and nearly 90 degrees for CFC and GFC, respectively. Hwang et al. [7]

investigated a novel approach for evaluating the material properties of filament-wound composite vessels with good results.

With the exception of the research by Hwang et al., much of the existing research uses current standard test methods including the unidirectional plate test (ASTM D3039), split disk method (ASTM D2290), and the hydraulic pressure test of filament-wound pressure vessels (ASTM D2585). For the testing of open-ended composite cylinders, all of these test methods have shortcomings that either introduce errors or make the testing more complicated and expensive. The unidirectional plate test uses composite fiber filaments wound around a flat plate mandrel to fabricate the test specimen and errors are inserted due to varying geometry and residual stresses compared to the actual cylinder whose properties are desired [7]. The split ring method introduces errors due to loading not being purely tensile during the test [7]. Although the hydraulic pressure test gives excellent results for pressure vessels, testing of the composite cylinders used for ADP testing would require capping the ends to allow pressurization with from an external source.

Horide et al. [8] successfully tested multi-ply GFC under internal pressure using a modified ring burst test that removed much of the errors seen with ASTM D2290. However, their test method requires a thin composite ring similar to the ASTM split ring specimen for testing. A patent search revealed several design for applying internal pressure to a cylinder [9-11]. All devices are similar in that they require a fluid to pressurize the test cylinder using either a high-pressure hydraulic pump or through application of a compressive force to a piston. These designs essentially cap the ends of the cylinder and require sometimes complex equipment to conduct testing. This study differs from prior research in that it explores a method to determine the material properties of a composite cylinder by directly testing the actual cylinder to failure without modification. This should remove errors due to uneven loading and scaling effects seen in prior research and testing standards.

THIS PAGE INTENTIONALLY LEFT BLANK

II.   TEST DEVICE DEVELOPMENT

A.   TEST DEVICE DESIGNS

In order to overcome the issues related to current systems designed to test hollow composite cylinders, two requirements for a new device were set. First, the device must be purely mechanical, requiring only a uniaxial testing machine for its use. Second, the device must be capable of testing cylinders without modification (i.e., capping the ends). These requirements result in an expansion device that converts the linear motion of a uniaxial testing machine to an expanding motion about the device's diameter to apply an internal pressure to the test cylinder.

Based on the aforementioned requirements for the test device, two designs were created. The first consists of a series of cylindrical segments connected by pins and rods to an upper and lower ram as shown in Figure 3. The test cylinder is placed around the device and coincident with the cylindrical segments. Each ram is then connected to the uniaxial testing machine, which, depending on the configuration of the device, applies either a tensile or compressive force to press the cylindrical wedges out against the test cylinder, thus applying the desired hoop stress.

Figure 3.   Cutaway View of Pin and Rod Design.

7

The second design, referred to as wedge and ram, created as a simpler alternative to minimize fabrication cost and difficulty. It consists of a series of cylindrical wedges with the inner faces cut at an angle of 80 degrees surrounded by an optional shim that acts as a spacer inside the test cylinder. Two rams with matching 80 degree conical surfaces mate with the inner surface of the wedges and a small guide rod is inserted in holes drilled on the facing surfaces of the rams to ensure proper alignment as shown in Figure 4 and Figure 5. As with the first design, the test cylinder is placed around the wedges and each ram is connected to a uniaxial test machine, which compresses the device. As the rams slide against the wedges, the angled inner surfaces force the wedges out and apply the desired internal pressure to the test cylinder.
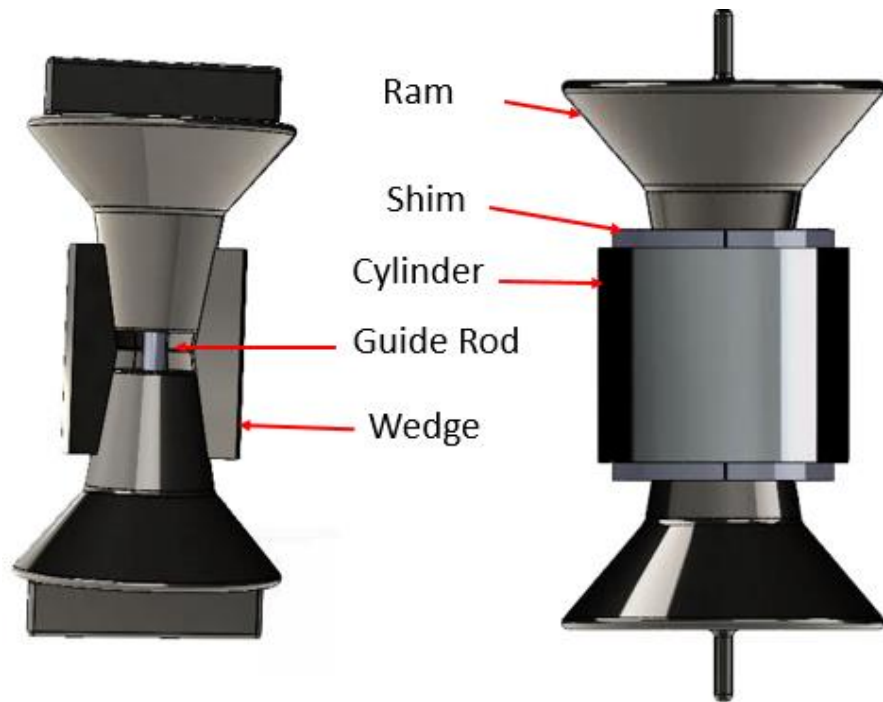
Figure 4.   Wedge and Ram Design.

Figure 5.   45 Degree Wedges as Fabricated, from [3].

The first design was determined to be impractical due to the size of the cylinders, 7.62cm (3in) diameter, to be tested. The relatively small inner diameter would lead to difficulties in fabrication and assembly of the device. Furthermore, due to stress concentrations at the pin connections, larger cross-sections than possible would be required in all parts to support the required loads. The second design, with its thicker cross-sections, is inherently stronger and simpler to fabricate and assemble due to its lack of moving parts. Based on this analysis, it was determined to continue with the second design for further testing.

B.   COMPUTER MODELING AND FINITE ELEMENT ANALYSIS

To validate functionality of the ram and wedge design, select an appropriate material, and for comparison with experimental testing, a computer model of the device was created and imported to ANSYS Mechanical Workbench for Finite Element Analysis (FEA). Simulations of two 6061 T6 aluminum cylinders with the following parameters were conducted:

- 7.62 cm (3 in) height

- 7.62 cm (3 in) inside diameter

- 0.3175 cm (0.125 in) and 0.635 cm (0.25 in) wall thickness hereafter referred to as thin and thick cylinders, respectively.

- Target hoop strains ranging from 0.001 to 0.01

- Friction coefficients of 0.01 (baseline), 0.05, and 0.1

1. Baseline Setup

After importing the test device and cylinder assembly, all contact areas between parts were defined as frictional surfaces with a friction coefficient of 0.01. The test cylinder was defined as 6061 T6 aluminum alloy [12] with constant strain hardening enabled to be more consistent with the nonlinear behavior of the experimental aluminum test cylinders while minimizing computation time. All test device components were initially defined as a general stainless steel. The assembly was then meshed using standard mesh controls with the exception of the cylinder and two wedges. For these components, the mesh was refined using a sweep method with 50 divisions and a face sizing refinement with five divisions. These modifications gave a more uniform and refined mesh throughout the thickness of the cylinder and wedges. The final mesh used for all simulations is shown in Figure 6. The various hoop strains to be modeled were defined with a vertical ramp displacement based on geometry on the top ram and a fixed support on the bottom ram to create the desired expansion of the wedges. The shim, tangs on the rams, and guide rod were removed from the simulation for simplicity since motion of the device was constrained to only the vertical axis as explained above.
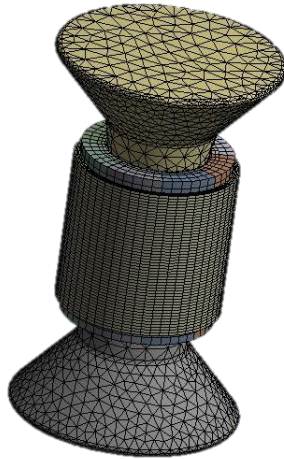
Figure 6.   Final Mesh Used for All Simulations Shown on the Thin Cylinder
Model.

2.   Baseline Results

The baseline results were initially used for checking functionality of the test device as well as for material selection. Based on a stress analysis of the test device components, 17–4 PH stainless steel in the annealed condition with a minimum yield strength of 1 GPa [13] was selected to prevent yield up to a minimum cylinder hoop strain of 0.01. The computer model stress versus target strain results for the wedge and ram are shown in Figure 7 and Figure 8, respectively. The target strain was computed from the geometry of the rams and wedges while neglecting their deformation. Maximum stress in both are well below the yield point of 17–4 PH stainless steel providing a factor of safety and allowing for future testing of stronger cylinders. Based on equivalent stress and maximum shear stress failure theories, the FEA model predicts failure at a cylinder hoop strains between 0.004 and 0.005. More detailed tabulated results from the FEA are available in Appendix B.
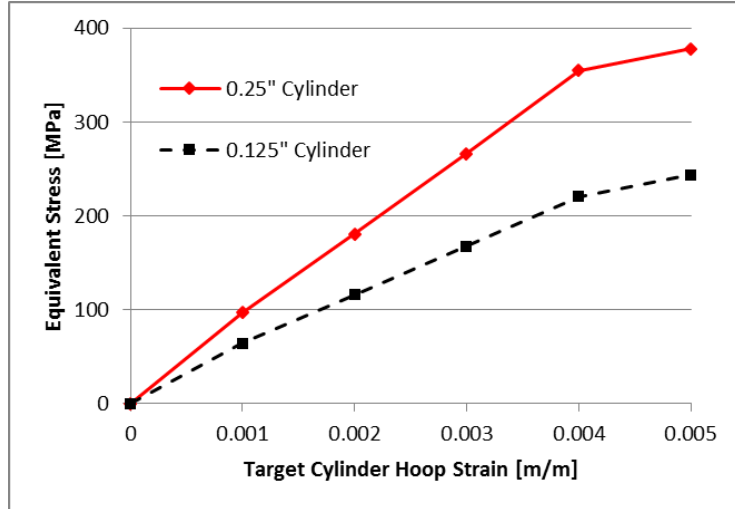
Figure 7.   Maximum Equivalent Stress in the Wedge for Thin and Thick
Aluminum Cylinders.
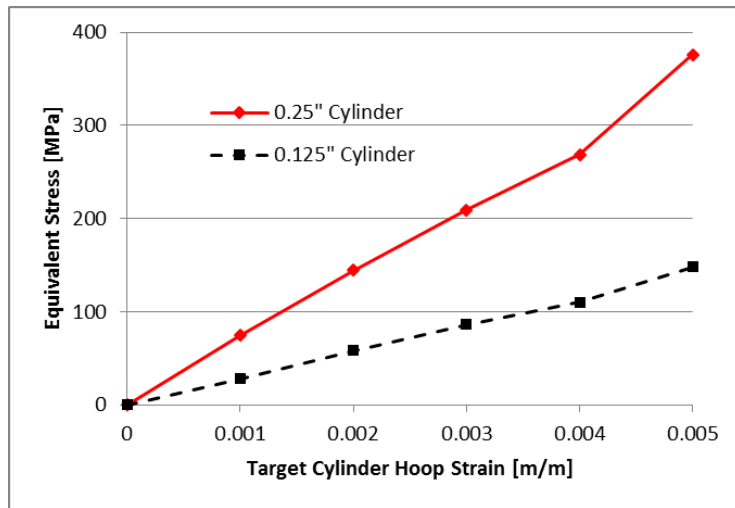
Figure 8.   Maximum Equivalent Stress in the Ram for Thin and Thick
Aluminum Cylinders.

Following material selection, the FEA hoop strain in the cylinder and maximum equivalent strain in the test device components were plotted against the target hoop strain for the thin cylinder as shown in Figure 9. The plot shows that the strains in the test device components when used with the thin aluminum cylinder are negligible and that the actual hoop strain in the test cylinder checks with the target value up to approximately 0.005 hoop strain where the model predicts plastic deformation leading to failure of the test cylinder. Error between target and actual hoop strain is less than 7.5% at target hoop

12

strains of 0.004 and below as shown in Table 1. Since strain gages will be used to measure actual hoop strain during the experimental tests, any difference between the target hoop strain based on ram motion and the cylinder's actual hoop strain are not important.
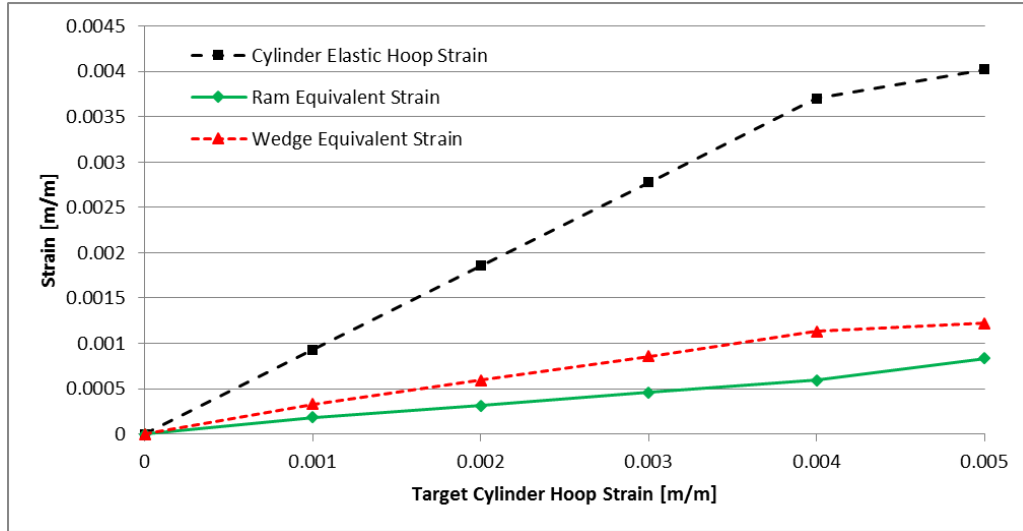
Figure 9.   Thin Cylinder Strain versus Target Cylinder Hoop Strain.

Table 1.   Thin Cylinder Finite Element Analysis Results.

Target Hoop Strain	0.001	0.002	0.003	0.004	0.005
FEA Hoop Strain	0.000931	0.001855	0.002779	0.003706	0.004024
Error	-6.92%	-7.28%	-7.37%	-7.36%	-19.53%

The above analysis was repeated for the thick aluminum cylinder and the FEA strain versus target strain results are shown in Figure 10 with a predicted hoop strain at failure of approximately 0.007. From this, it is immediately apparent that the strain in the ram and wedge of the test device are more significant than when testing the thin aluminum cylinder. As a result, the error in actual versus target hoop strain is higher at approximately 35% as shown in Table 2. Although the error between target and actual hoop strains is unimportant since strain gages will record the hoop strain for future calculations, the more significant strains in the test components may have a detrimental

effect on the capability of the test device to apply sufficient internal pressure to cause failure prior to reaching the limits of the device.
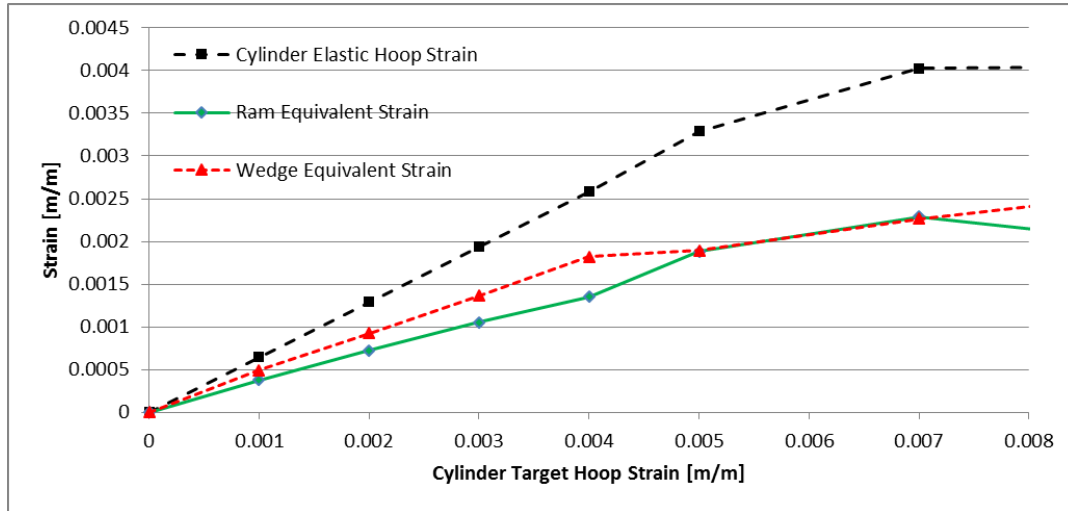
Figure 10.   Thick Cylinder Strain versus Target Cylinder Hoop Strain.

Table 2.   Thick Cylinder Finite Element Analysis Results.

Target Hoop Strain	0.001	0.002	0.003	0.004	0.005
FEA Hoop Strain	0.000647	0.001292	0.001938	0.002584	0.003288
Error	-35.33%	-35.39%	-35.40%	-35.39%	-34.24%

A Satec uniaxial compression-testing machine of model MII-20UD with a 200 kN load capacity was to be used for all cylinder tests. To ensure that the Satec machine had sufficient capacity for achieving the desired hoop strains, the required compressive machine force was plotted against each target cylinder hoop strain value in Figure 11. As expected, the compressive force required for a given hoop strain significantly higher for the thick cylinder however with a maximum required compressive force of less than 150 kN, all target strains are within the capacity of the Satec testing equipment.
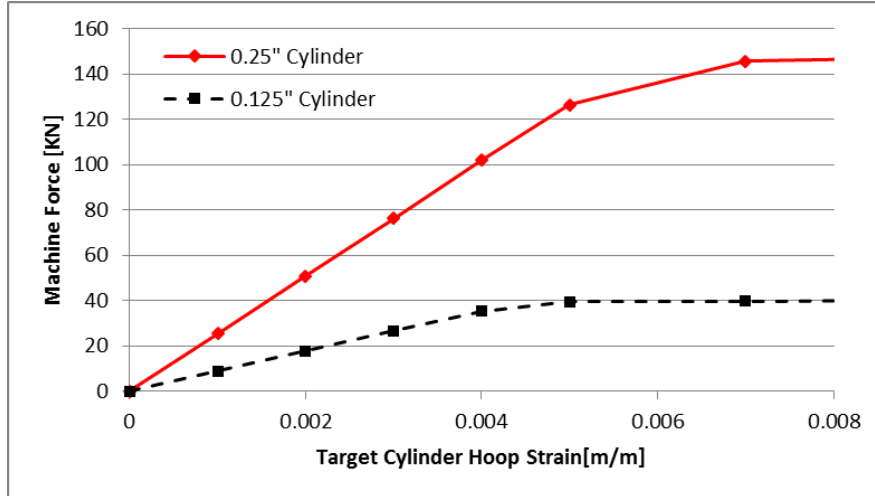
Figure 11.   Required Compressive Machine Force Versus Target Cylinder Hoop
Strain.

Due to the segmented design of the wedges, consisting of eight 45 degree wedges, there will exist some non-uniformity of stress applied to the cylinder, especially at the interface between wedges. Figure 12 shows the degree of non-uniformity with a fairly constant stress across each wedge and lower stress at each wedge interface.
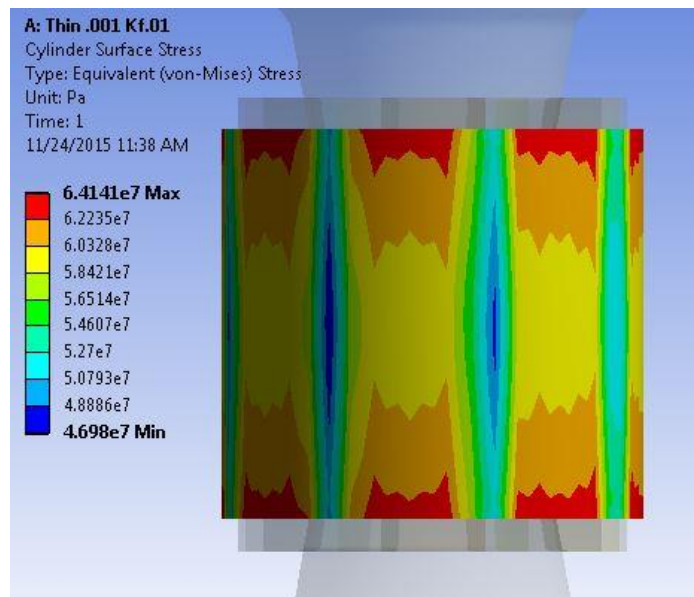
Figure 12.   Equivalent Stress on the Outer Surface of the Thin Aluminum
Cylinder at a Target Hoop Strain of 0.001.

To understand the degree of non-uniformity across the wedge better, the hoop strain was plotted against the location relative to a wedge for the thin and thick cylinders in Figure 13 and Figure 14. While the strain distribution for the thin cylinder is fairly uniform except for the five degrees on either side of the wedge, the thick cylinder shows more variation across the entire wedge.
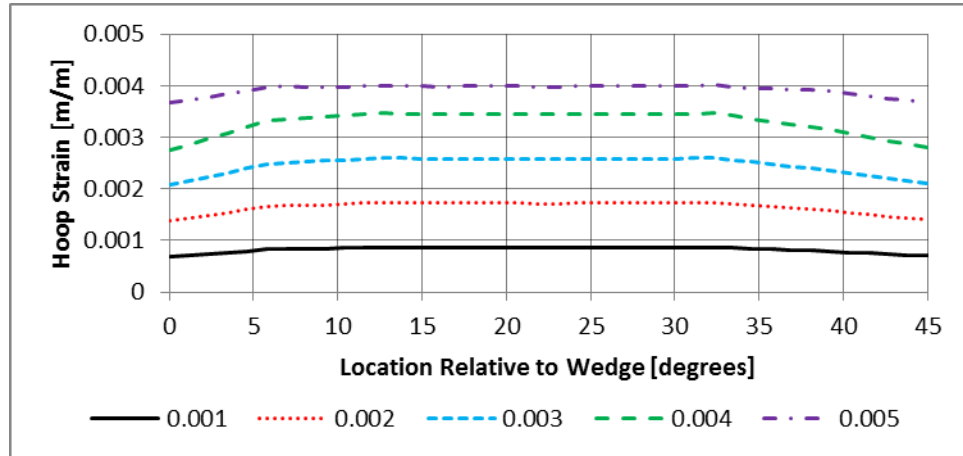
Figure 13. Hoop Strain versus Location Relative to Wedge for the Thin Cylinder.
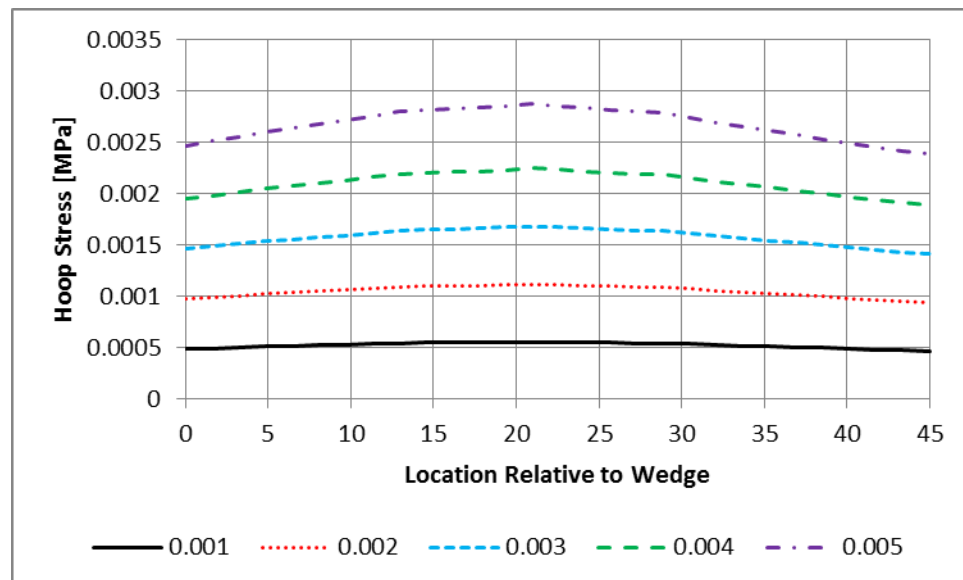
Figure 14. Hoop Strain versus Location Relative to Wedge for Thick Cylinder.

16

As a final validation of the FEA results, thin and thick cylinder equations were used for comparison with the FEA results for the thin aluminum cylinder. Thin-walled assumptions are considered valid when the ratio of radius to thickness is greater than 10. The thin aluminum cylinders and composite cylinders have a ratio of approximately 12 while the thick aluminum cylinder has a ratio of six. To derive the equations, it was necessary to determine equations for the cylinder inner pressure and hoop strain as a function of the friction coefficient and applied machine force. Two free body diagrams were created representing a ram and a wedge as shown in Figure 15 and Figure 16. From the two free body diagrams, a force balance was calculated resulting in thin and thick cylinder equations for cylinder hoop strain at the outer surface as a function of an assumed friction factor and applied machine force.
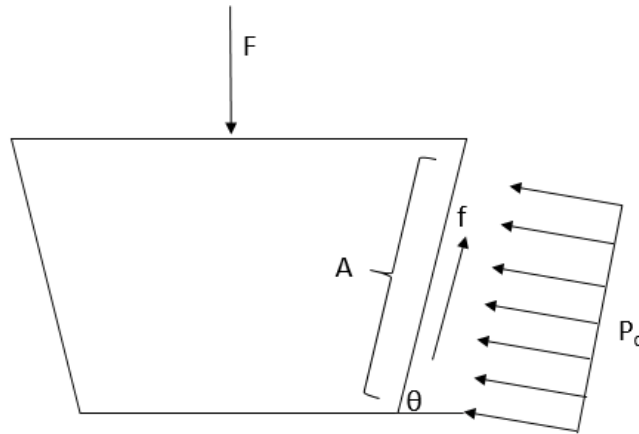
Figure 15.   Free Body Diagram for a Ram.
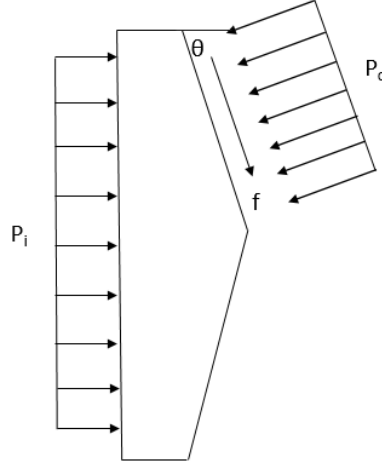
Figure 16.   Free Body Diagram for a Wedge.

Equation 1 uses thin cylinder assumptions while Equation 2 uses thick cylinder assumptions to relate the applied machine force and friction coefficient to the cylinder hoop strain. In Equation 1, L and t are the cylinder length and wall thickness respectively. In Equation 2; a, b, and L are the inner radius, outer radius, and cylinder length, respectively.

$$\varepsilon_\theta = \frac{F}{\pi E L t} \frac{\tan\theta - \mu}{1 + \mu\tan\theta} \tag{1}$$

$$\varepsilon_\theta = \frac{2a^2 F}{\pi R L E (b^2 - a^2)} \frac{\tan\theta - \mu}{1 + \mu\tan\theta} \tag{2}$$

A MATLAB script was developed to perform the above calculations for the thin aluminum cylinder and is available in Appendix A. The average hoop strain across the wedge from the finite element analysis was then compared to the analytic values in Table 3. The FEA results correspond well with the analytical results, providing a final validation of the finite element analysis predictions.

Table 3.   Finite Element and Analytic Hoop Strain.

Target Hoop Strain	0.001	0.002	0.003	0.004	0.005
FEA	0.000824	0.001646	0.002469	0.003292825	0.003927
Analytic thin cyl equations	0.0009	0.0018	0.0026	0.0035	0.0039
Error	-8.47%	-8.55%	-5.03%	-5.92%	0.68%
Analytic thick cyl equations	0.0008	0.0016	0.0023	0.0031	0.0035
Error	2.97%	2.89%	7.36%	6.22%	12.19%

3.   Varying Friction Results

An important part of the experimental analysis will be accurately determining the friction coefficient between the rams and wedges. To determine the effect of varying levels of friction on the test device as well for comparison with experimental results, the baseline finite element analysis was repeated with three different friction coefficients ranging from baseline to 0.1. The only significant different between the various simulations was the required compressive machine force at a given target hoop strain. Since friction tends to oppose the compressive force applied by the machine, any increase in friction will result in a larger compressive force required for a given hoop strain as shown in Figure 17.
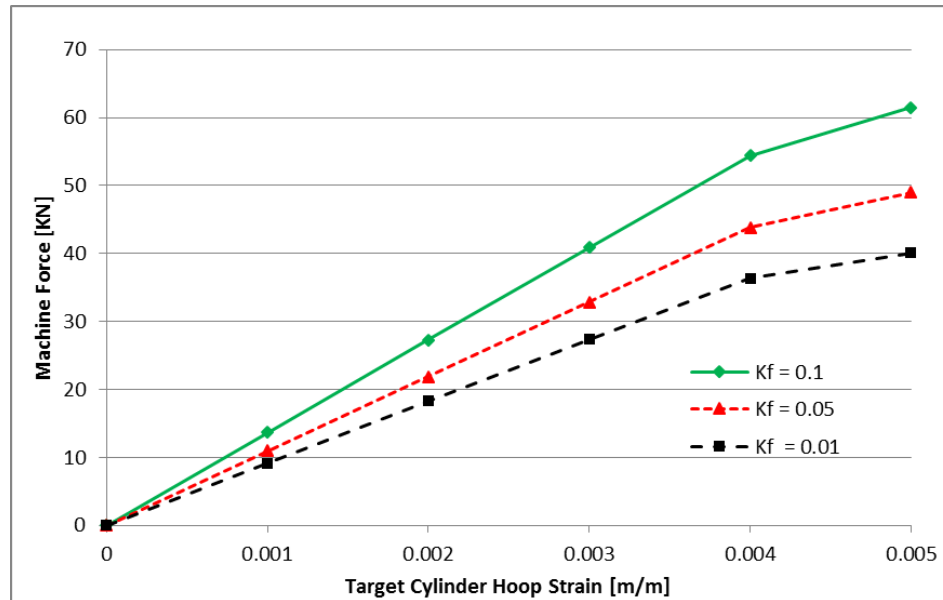
Figure 17.   Machine Force versus Target Hoop Strain for Various Coefficients of Friction

THIS PAGE INTENTIONALLY LEFT BLANK

III.   EXPERIMENT

A.   COMPOSITE CYLINDER FABRICATION

Composite cylinders were made with continuously wound strips of both glass fiber and carbon fiber woven fabrics, epoxy resin, and hardener. For consistency between cylinders, a mold was designed to ensure a consistent inner diameter of 7.62 cm (3 in). For testing, the Glass Fiber Composite (GFC) and Carbon Fiber Composite (CFC) cylinders were fabricated with a nominal wall thickness of 0.3175 cm (0.12 in) corresponding to approximately five and six layers of wrapping, respectively.

1.   Mold Setup

The mold was created entirely from off-the-shelf parts. The cylinder form around which the fabric strips will be wound consists of a 30.48 cm (12 in) long hollow aluminum tube. Two standard metal shelf supports were mounted to a sheet of wood to create a support base for the cylinder form. A large wood dowel was then inserted into the aluminum tube and screws were used to connect the cylinder form to the support base as shown in Figure 18.
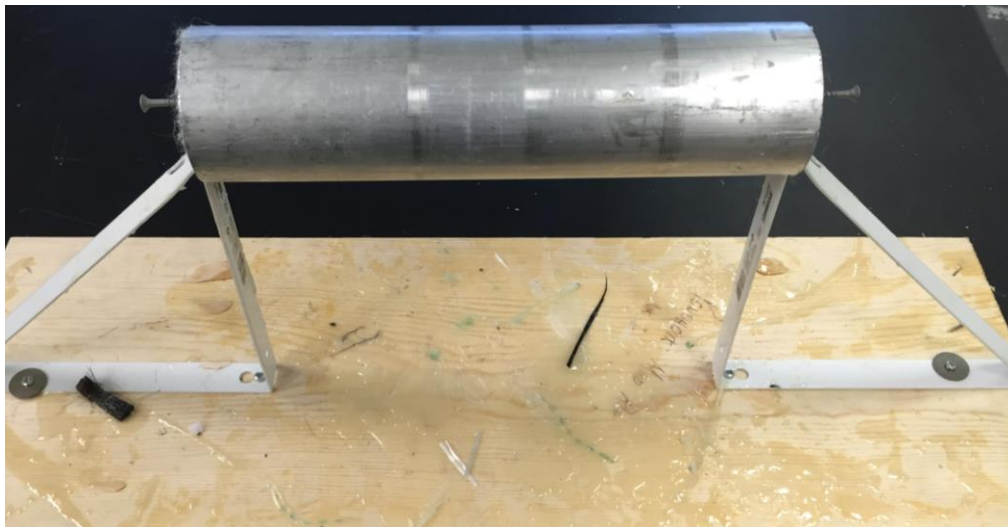
Figure 18.   Cylinder Mold Prior to Preparation for Composite Layup.

To prepare the mold for composite layup, a layer of release ply paper followed by a layer of Teflon sheet were wrapped around the aluminum cylinder form. The two layers prevent any epoxy from sticking to the form and ensuring an easy release following curing. Next, two rubber drain pipe couplers were used to create top and bottom guides for composite strip alignment as well as an outer surface forms for the composite cylinders. The top and bottom guides were made by cutting the rubber coupler into two narrow strips of the correct diameter and then wrapping them around the mold cylinder to contain the fiber fabric during wrapping. The second coupler was left at its original length of 10.16 cm (4 in) but cut to a circumference of 25.9 cm (10.2 in) to match the outer circumference of the cylinders to be fabricated. A mold prepared for cylinder layup is shown in Figure 19.
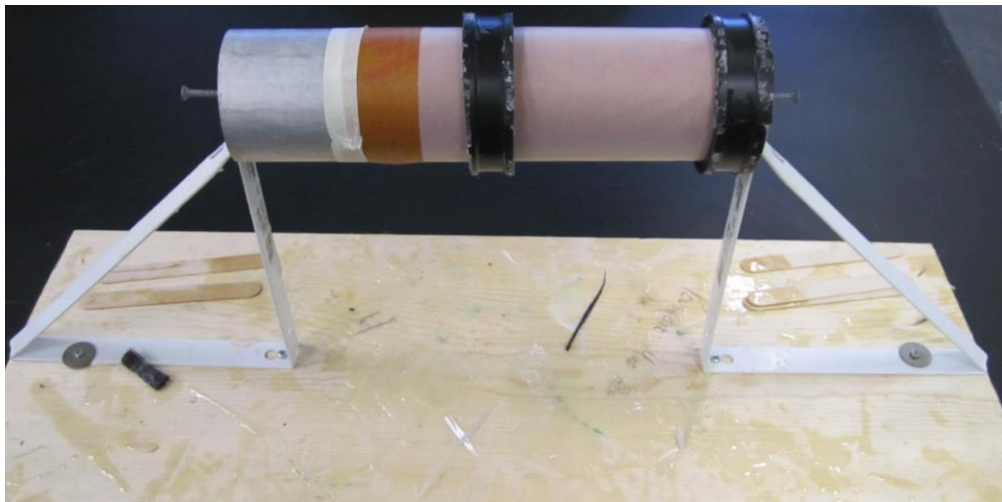
Figure 19.   Cylinder Mold Prepared for Composite Cylinder Layup.

2. Composite Layup

To prepare for layup, the needed supplies were first gathered. These include PRO-SET M1002 resin, PRO-SET M2043-1 hardener, mixing cup, scale, stir stick, brush and roller as shown in Figure 20. For use following composite wrapping, 10.16 cm (4 in) wide strips of perforated release ply and breather cloth, two vacuum bags, and double sided tape were prepared as shown in Figure 21.

Figure 20.   Composite Layup Supplies.
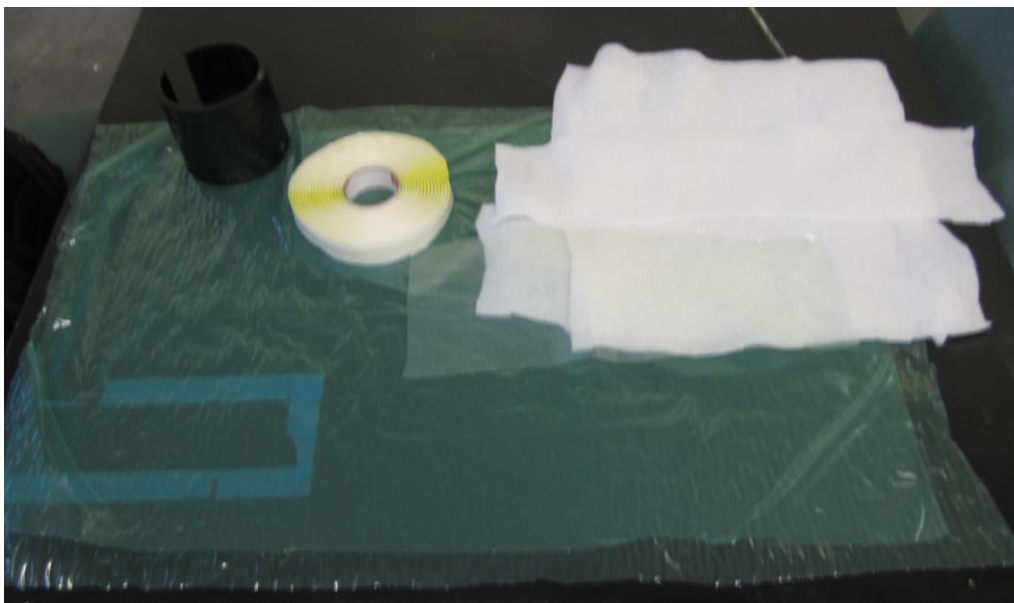
Figure 21.   Additional Composite Layup Supplies

To begin layup, the resin and hardener were thoroughly mixed in a 4.17 by weight ratio. For both glass and carbon fiber composites, 80 and 19.18 grams of resin and hardener, respectively, provided the correct amount of epoxy while to provide full

coverage while minimizing waste. Following mixing, the epoxy was applied to either side of the first 25 cm (9.84 in) of the strip as well as the mold rig. This initial application ensures compete epoxy coverage for the first wrap of the fiber strip to minimize voids during the curing process. Next, the strip was hand-wrapped around the mold cylinder between the two rubber guides. Additional epoxy was applied between each layer of the wrap using the brush and spread evenly with the roller. Maintaining tension on the fiber strip during the wrapping process is key to fabricating a uniformly thick cylinder with minimal voids. Figure 22 shows a carbon fiber composite cylinder just after wrapping and prior to vacuum bagging.
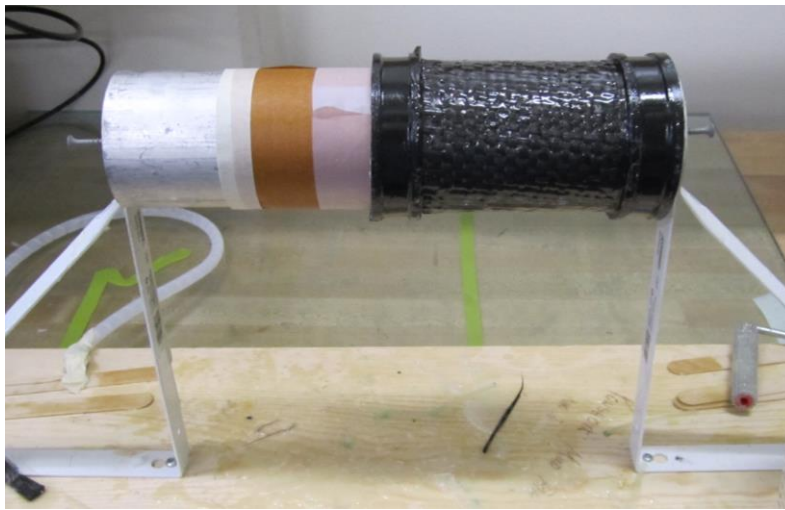
Figure 22.   Carbon Fiber Composite Cylinder Immediately after Wrapping.

The next step in fabrication was wrapping the composite cylinder with the pre-prepared strip of perforated release ply and breather cloth. The breather cloth absorbs any excess epoxy that is pressed through the perforated release ply. A spiral-wound line connected to a vacuum pump was then taped to the mold cylinder as shown in Figure 23. The entire mold cylinder was then removed from the base and wrapped in breather cloth to absorb excess resin and prevent the edges of the aluminum mold cylinder from cutting into the vacuum bag. Finally, the mold cylinder was placed in a vacuum bag and under 20–25 in hg vacuum as in Figure 24 for 1.25-1.5 hours to allow the curing process to begin.

Figure 23.   Composite Mold Wrapped with Breather Cloth and Vacuum Line Attached.

Figure 24.   Cylinder Mold Removed from Base and Placed Under 508-635 mm Hg (20–25 in Hg) Vacuum.

Following the initial cure time, the vacuum bag, breather cloth, and perforated peal ply were removed from the composite cylinder and mold allowing for inspection of the partially-cured cylinder seen in Figure 25. A roller was used to smooth the outer surface before placing the rubber outer form around the composite cylinder and wrapping tightly with electrical tape. The mold was then again wrapped with perforated release ply and breather cloth and placed in a vacuum bag for an additional three hours under 508-635 mm Hg (20–25 in Hg) vacuum to allow for complete curing of the epoxy resin.

Figure 25.   Carbon Fiber Composite Cylinder Following Initial 1.25-1.5 Hour Cure.

3.   Cylinder Finishing

Following the final cure, the composite cylinder and the mold were removed from the vacuum bag, breather cloth, and perforated peel ply. A section of PVC pipe was then used as a ram to remove the composite cylinder from the mold as shown in Figure 26**.** Following removal from the mold, the top and bottom guide and the outer surface form were removed from the composite cylinder resulted in the rough cylinder in Figure 27**.**
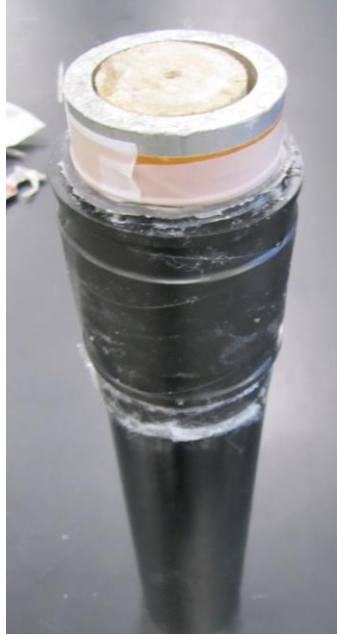
Figure 26.   Cured Composite Cylinder with PVC Removal Ram.
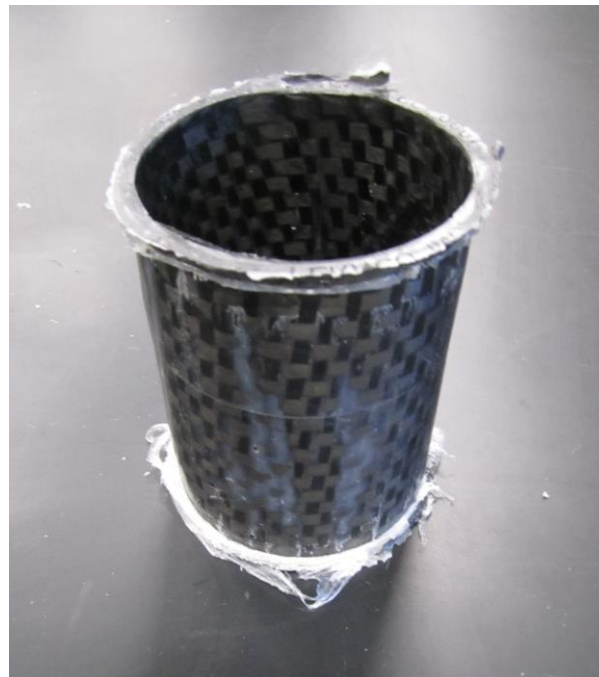
Figure 27.   Rough Carbon Fiber Composite Cylinder after Removal from Mold.

As a final step to create uniform cylinders, a rotary cutting tool was used to trim the top and bottom of each rough composite cylinder to create nominal finished composite cylinders 7.62 cm (3in) tall, with a 7.62 cm (3 in) inside diameter, wall thickness of 0.316 cm (0.125 in) for testing. Figure 28 and Figure 29 show typical finished glass and carbon fiber composite cylinders.

Figure 28.   Typical Finished Glass Fiber Composite Cylinder.

Figure 29.   Typical Finished Carbon Fiber Composite Cylinder.

B. COMPOSITE TENSILE SPECIMEN FABRICATION

Square CFC composite sheets were prepared for fabrication of tensile specimens of the dog-bone shape. For comparison purposes, the sheets were fabricated to have a nominal thickness of 0.3175 cm (0.12 in) by using six layers of composite to match the CFC cylinders previously discussed.

1. Composite Layup

To prepare for layup, the needed supplies were first gathered as with the composite cylinder fabrication except instead of strips of composite weave, six 47 cm by 47 cm squares of CFC were cut to create a six-ply CFC plate.

To begin layup, the resin and hardener were thoroughly mixed in a 4.17 by weight ratio as with the composite cylinder layup. Following mixing, the epoxy was applied to either side of the first CFC square to ensure complete coverage for the first ply. The remaining CFC squares were applied one at a time with epoxy spread and rolled between each layer to adequately spread the epoxy and remove air bubbles.

The completed six-ply sheet was then covered with a layer of perforated release ply and breather cloth to absorb excess epoxy. A spiral-wound line connected to a vacuum pump was routed along the edge of the CFC sheet and taped to the table. Double-sided tape was used to frame the spiral-wound line and a layer of vacuum bag was placed over the CFC sheet and attached to the double-sided tape as shown in Figure 30. The vacuum pump was energized and the system was maintained at 508-635 mm Hg (20–25 in Hg) vacuum for 4.5-5 hours for a complete cure.
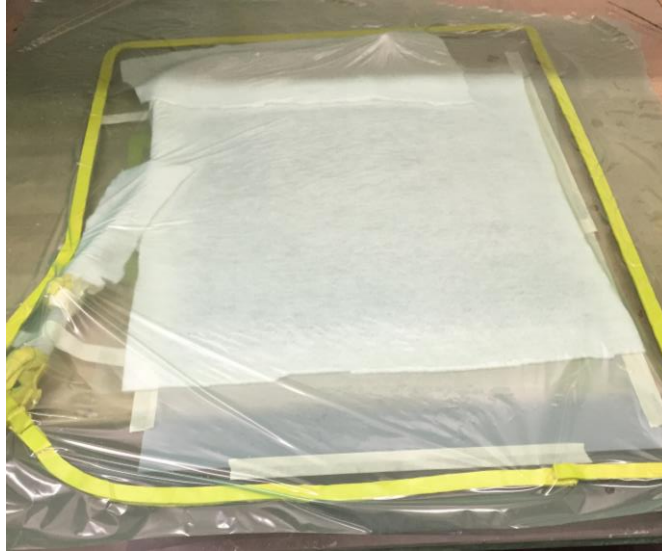
Figure 30.   Carbon Fiber Composite Sheet Layup Prior to Applying Vacuum.

2.   Tensile Specimen Finishing

After curing, the CFC sheet was cut into coupons in preparation for tensile testing. Although composite tensile testing typically uses a specimen with a rectangular profile [14], it was decided to use the more smoothly curved tensile specimen profile prescribed for plastics [15] in an attempt to prevent failure of at the grip of the testing machine. A typical CFC tensile specimen is shown in Figure 31.

Figure 31.   Carbon Fiber Composite Tensile Specimen.

C.   STRAIN GAGES

Strain gages were used to measure the hoop and longitudinal strain of the test cylinders at various locations on the cylinder and for the CFC tensile specimens. The first set of tests consisted of one of each type of cylinder: thin aluminum, thick aluminum, fiberglass, and carbon fiber composite. To determine the uniformity of the applied hoop

stress, four uniaxial strain gages were applied in the hoop direction at each wedge interface and centered on each wedge. The remaining cylinders utilized two 90 degree strain gage rosettes and a single uniaxial strain gage in the hoop direction. For the tensile specimens, a single 90 degree rosette was placed on the gage length. Although testing standards call for strain gages mounted on either side of the specimen when determining Young's modulus [14], only a single rosette was used due to strain gage supply limitations. The 90 degree rosette strain gages were Micro-Measurements part number CEA-13-125WT-350. The uniaxial strain gages were Omega part number SGD-7/350-LY4.

1.   Application of Strain Gages

The following procedure was used to apply strain gages to all test cylinders.

1.   Prepare Surface: The location for each strain gage was smoothed with a fine grit sand paper to remove imperfections. Following sanding, the surface was cleaned using a gauze pad soaked with ethanol followed by another gauze pad soaked with methanol.

2.   Place Strain Gage: A small piece of cellophane tape was applied to the strain gage location and the used to hold the strain gage in place during curing.

3.   Apply Bonding Agent: A Micro-Measurements M-Bond AE-10 Adhesive kit containing a two-part epoxy, dropper, and stir stick was used to bond the strain gages to the cylinder. The dropper was used to measure the appropriate amount of hardener for mixing with the resin for the designated five minutes. Following mixing, the stir stick was used to apply a small amount of epoxy to the strain gage. The strain gage and tape were then firmly pressed onto the cylinder.

4.   Wire leads: Following a 48 hour cure, the tape was removed and a dental tool was used to remove an excess resin from the solder pads on the strain gage. The lead wires were then soldered to the pads on the strain gages. Figure 32 shows a cylinder with wired strain gages attached.

Figure 32.   Aluminum Cylinder Shown with Two 90-degree Strain Gage
Rosettes Wired for Testing.

D.   TESTING PLAN

The initial goal of the experiment was to validate the test device's capability to apply an internal pressure to various hollow cylinders to failure. Once validated, the remaining cylinders were tested to determine the coefficient of friction between the ram and wedge and to experimentally determine the elastic modulus and burst pressure of the GFC and CFC cylinders. Finally, several CFC tensile specimens were tested to provide a second means of determining the CFC's elastic modulus as a check against the value found using the test device. The complete testing plan with specific strain gage setup is shown in Table 4.

Table 4.   Complete Test Plan.

Run	Description	Data	Strain Gage	Rate
Thin Al 1	Machined Aluminum Cylinder	Force Strain	1	2 mm/min extension
Thin Al 2				
Thin Al 3	As Received Aluminum Cylinder		2	
Thin Al 4				
Thin Al 5				
Thin Al 6				
Thick Al 1	Machined Aluminum Cylinder		1	
Thick Al 2				
GFC 1	GFC Cylinder		2	
GFC 2			1	
GFC 3			2	
CFC 1	CFC Cylinder		1	
CFC 2			2	
CFC 3			2	
CFC 4			2	
CFC T1	CFC Tensile Specimen		3	
CFC T2			3	
CFC T3			3	
*1	4 x uniaxial in hoop direction			
*2	2 x 90 deg rosette and 1 x uniaxial in hoop direction			
*3	1 x 90 deg rosette			

E.   PROCEDURE

Before each test run, the wedge and ram contact surfaces were coated with a thin coat of high pressure Lithium-Moly grease to minimize friction and minimize variation between test runs. The test cylinder was then placed around the device and the entire assembly placed between the pads of the 200 kN Satec uniaxial testing machine. The strain gages were then connected to the data acquisition system as shown in Figure 33.

Figure 33.   Test Device and Cylinder Assembly Prepared For Test Run.

After lowering the crosshead of the uniaxial testing machine until contact with the test device was achieved, the machine's extension was zeroed and its force balanced. Next, the gage factor of the strain gage was entered into the data acquisition system and each gage was calibrated. With the setup complete, the test was initiated by starting the testing machine and data acquisition software. The test was complete after cylinder failure or when the test device reached maximum expansion, whichever occurred first. The log files from both the data acquisition system and testing machine, consisting of strain and force data, were then exported for analysis.

Test setup for the CFC tensile specimens was similar to that for the cylinders. The tensile specimen was placed in an Instron model 4507 uniaxial testing machine and attached with grips at the top and bottom. The machine's crosshead extension was then

zeroed and its force balanced. After connecting the strain gages to the data acquisition system, their gage factor was entered and the gages were calibrated. As with the cylinder tests, the tensile test runs were initiated by starting the testing machine and data acquisition software. The test was complete once the tensile specimen failed. The log files containing strain and force data were then exported for analysis.

THIS PAGE INTENTIONALLY LEFT BLANK

IV. RESULTS

A. THIN ALUMINUM CYLINDER

Six thin aluminum cylinders were prepared for testing by attaching strain gages. All were successfully tested to failure using the test device however, data for thin aluminum cylinders #2 and #3 were corrupted by the data acquisition system. Thin aluminum #1 was machined to the proper test cylinder dimensions so its results are not compared to thin aluminum #4-6 since they were tested as-received by the manufacturer.

1. Results

The machine force versus strain curves for the two functioning channels for run #1 are shown in Figure 34. The other two hoop strain gages became disconnected due to poor solder joints early in the test and their data was discarded. The negative hoop strains below approximately 10 kN of machine force were attributed to poor alignment of the strain gages with both being off the hoop axis by approximately 10 degrees. Above that point, the curves are as expected for an aluminum cylinder and show a fairly linear elastic region with a smooth transition to the plastic region as expected for aluminum. The larger strain observed in channel one is due to its location nearer the failure point along with it being centered on a wedge. Channel 1 was opposite the failure location, centered on a gap, and recorded about half the strain as channel 2 throughout the test. This corresponds with the finite element analysis that predicted a lower hoop strain at wedge interfaces although the difference was larger than expected. Small variations in the cylinder wall thickness as well as strain gage misalignment could be a contributing factor to the difference recorded by both channels. The average hoop strain at failure was 0.00616 and was higher than that predicted by the finite element model. The difference between the observed failure strain and the predicted 0.005 failure hoop strain was attributed to an insufficient number of channels recorded for averaging as well as the misalignment of the strain gages that did record.
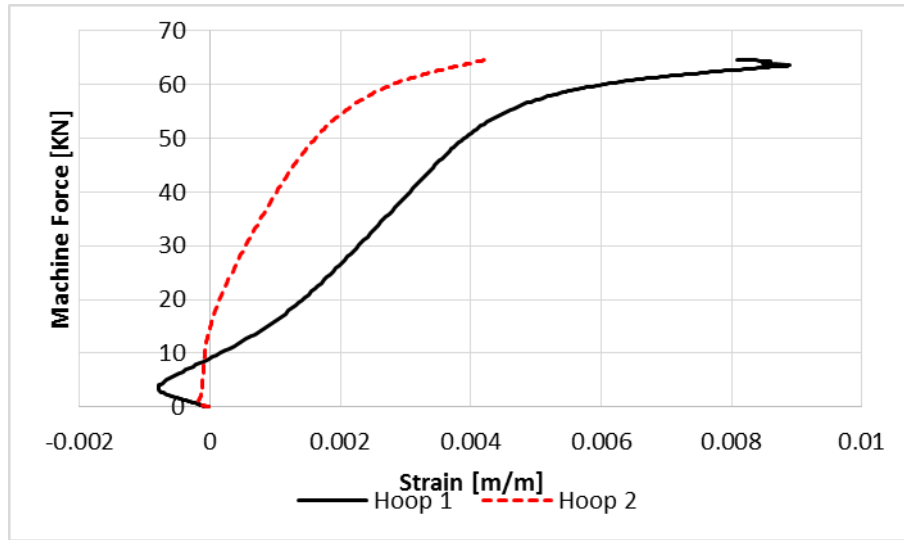
Figure 34.　Thin Aluminum #1 Test Results.

Figure 35 shows the test cylinder failure location along with the strain gage corresponding to hoop 1. While the failure was vertical as expected due to hoop stress applied, it did not travel the entire length of the cylinder. Uneven insertion of the rams to a small degree was attributed as the cause of the asymmetric failure line.

Figure 35.　Failure of Thin Aluminum #1 Near Hoop Strain Channel 1.

Thin aluminum #4 was successfully tested to failure and the results are shown in Figure 36. All measured channels showed good correlation with less spread than was observed during the testing of thin aluminum #1. Hoop 2 was nearest the failure location,

centered on a wedge, and had the highest recorded strains throughout the test as predicted by finite element analysis. Hoop 3 was centered on a gap and displayed the lowest hoop strains throughout the test as predicted. Furthermore, all channels show a very linear elastic response up to hoop strains of 0.002 with a smooth transition to the plastic region as expected for aluminum. Additionally, the hoop and axial strain channels were both averaged to determine a Poisson's ratio equal to 0.33 for this test cylinder which matches the expected value for 6061 T6 aluminum used for the cylinder.
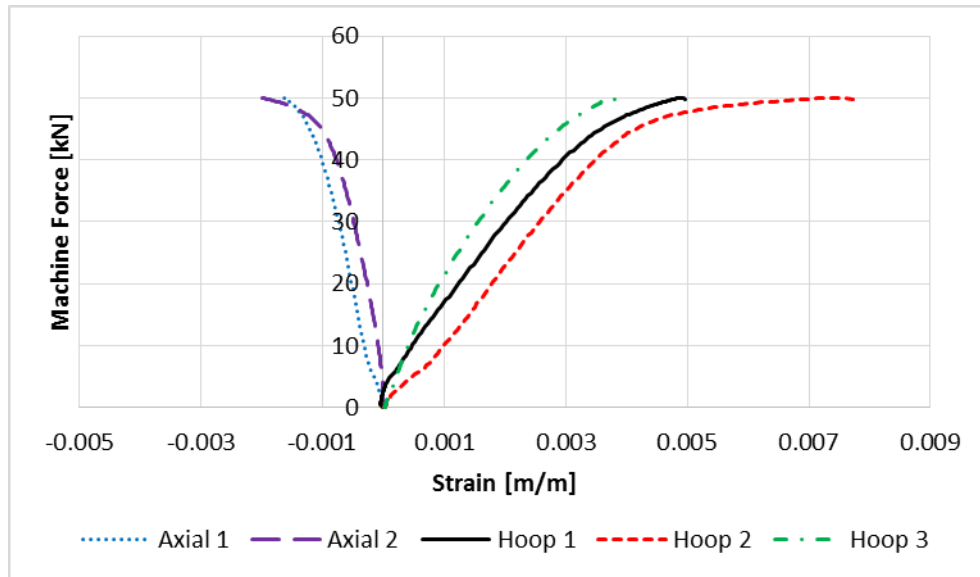
Figure 36.   Thin Aluminum #4 Test Results.

The failure of thin aluminum #4 was similar in appearance to that oberved with thin aluminum #1 as shown in Figure 37. As before, the failure is vertical however it does not travel the entire height of the cylinder. Additionally, some necking is visible at the top of the cylinder centered on the failure location. Along with the crack being wider at one end, these observations are indicative of some asymmetry in the motion of the upper and lower rams causing more expansion on one end of the cylinder than the other. Additionally, variation in wall thickness and material properties throughout the cylinder could contribute to the asymmetric failure.

Figure 37. Failure Location of Thin Aluminum #4 Near Strain Channel 2.

Thin aluminum #5 was successfully tested to failure and the results are shown in Figure 38. Strain channels 2 and 3 show a good correlation and correspond to locations centered on wedges. Additionally, hoop 2 was closest to the failure location and shows the highest strain throughout the majority of the test. Hoop channel 1 recorded lower strains throughout the test however this was expected since it was centered on a gap. While a transition from linear elastic response to nonlinear plastic response is still apparent for channels 1 and 2 above hoop strains of 0.002, the transition is not as clear as that observed for thin aluminum #4 in Figure 36. An average Poisson's ratio of 0.43 was calculated by averaging all strain channels. This is higher than the expected value of 0.33 and the difference is likely due to the lower strain recorded by channel 1. Removing hoop 1 from the calculation brings the experimentally found Poisson's ratio to 0.36 corresponding to a 9% error from expected.
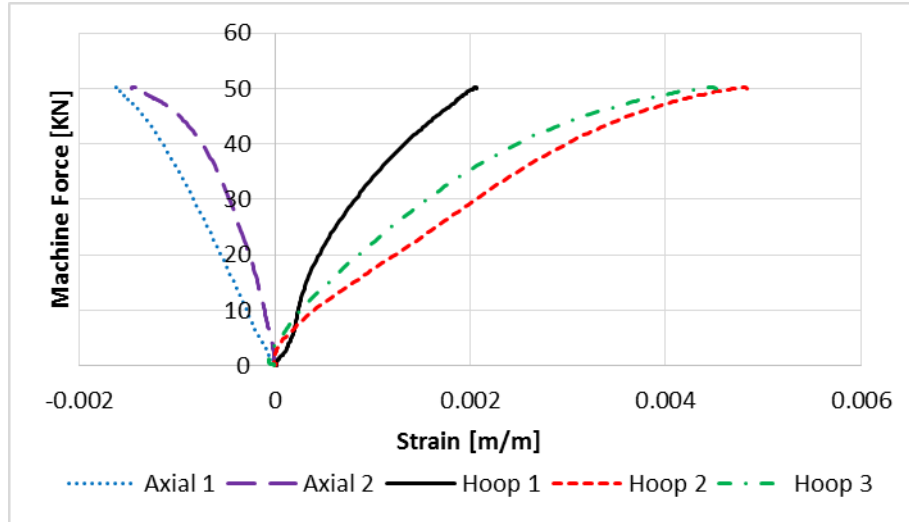
Figure 38.   Thin Aluminum #5 Test Results.

Thin aluminum #5 and its failure location are shown in Figure 39. As with the previous thin aluminum cylinders, the crack did not travel the entire length of the cylinder. The shape of the crack indicates that it initiated at the top of the test cylinder and traveled downwards from there. As was observed with the previous thin aluminum tests, this indicates that there is a level of asymmetry in the movement of the rams resulting in more expansion at one end of the cylinder than the other. Hoop 1 recorded strains smaller by a factor of two throughout the test compared to the other strain channels. While it was centered on a wedge gap, the difference is larger than predicted by FEA. As with thin Aluminum #1, variation in wall thickness and material properties likely contributed to the small measured hoop strain on channel 1.

Figure 39.   Failure Location of Thin Aluminum #5 Near Strain Channel 2.

Thin aluminum #6 was successfully tested to failure and the results are shown in Figure 40. The hoop strains for this test run showed more spread than was observed with thin aluminum #4 and #5 although the results still correlate qualitatively with expected values. Channel 1 was nearest the failure location as well as centered on a wedge and recorded the highest hoop strain throughout the test. Channel 3 on the other hand, was furthest from the failure location as well as centered on a gap and recorded the lowest hoop strains. As with the previous thin aluminum tests, the highest recorded strain was near the failure location and centered on a wedge while the lowest strains were further from the crack location and centered on a gap between the interfaces of two wedges as predicted by finite element analysis. Calculation of Poisson's ratio by averaging the hoop and axial strains returned 0.39, a 19% error from the expected value of 0.33.
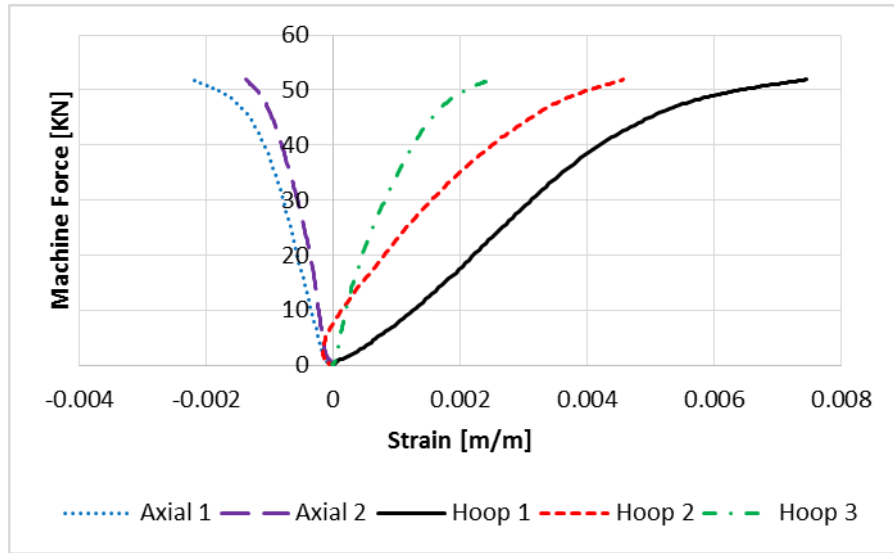
Figure 40.   Thin Aluminum #6 Test Results.

Thin aluminum #6 after testing is shown in Figure 41. In this case, the crack did progogate the entire length of the cylinder. However it is clear that the crack initiated at the top of the cylinder and progogated down towards the bottom. As with previous cylinders, a small amount of necking was observed centered on the crack on the bottom end of the cylinder oppposite from where the crack initiated. This was again determined to be caused by a small non-uniformtiy in the motion of the rams resulting in more internal pressure being applied on one end of the cylinder than the other.

Figure 41.   Failure Location of Thin Aluminum #6 Near Strain Channel 1.

To compare the results from thin aluminum #4 through #6, which were all made of 6061 T6 aluminum and tested cut to length in the as-received condition with no machining, the results for all strain channels of each run were averaged and plotted in Figure 42. The averaged results show excellent repeatability with a machine force at failure of approximately 50 kN and a failure hoop strain of approximately 0.005. Furthermore, the hoop strain response is linear up to 0.002 where a transition to nonlinear plastic behavior is observed as expected with aluminum. The tabulated averaged values for thin aluminum #4 through #6 at failure are shown in Table 5. Of particular interest is the similarity of the machine force at failure, which varies by less than 5% between the three runs. As a result, it was determined that the recorded data from thin aluminum #4 through #6 could be used to accurately determine the coefficient of friction between the ram and wedges and is discussed in the following section.
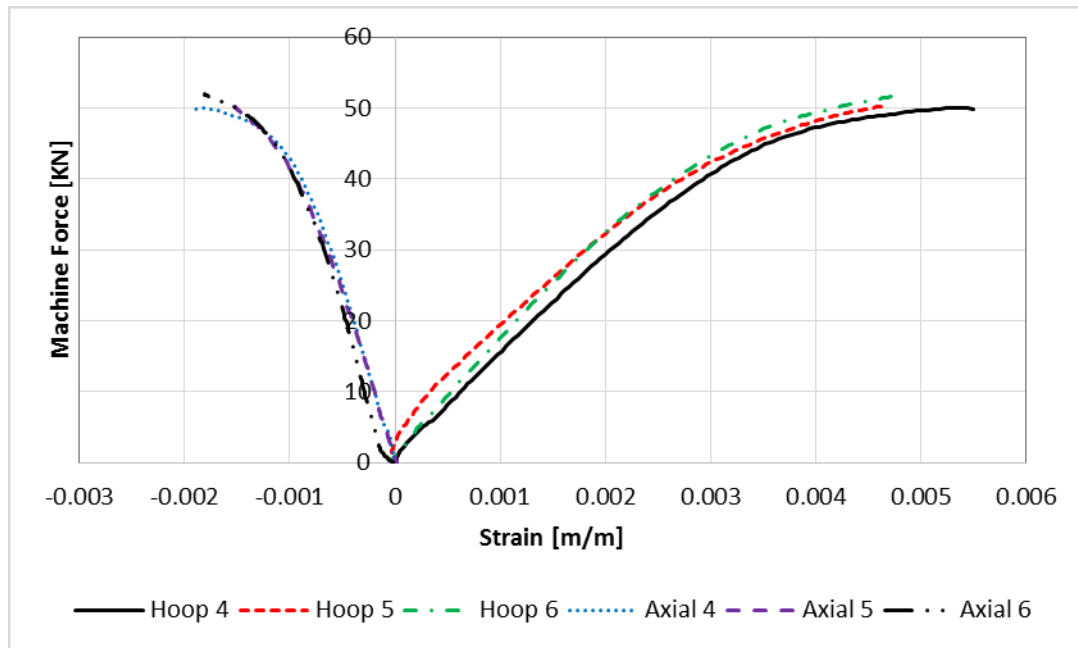
Figure 42.   Averaged Results from Thin Aluminum 4–6

Table 5.   Tabulated and Averaged Results for Thin Aluminum 4 through 6 at
Failure.

Run	Force	Hoop Strain	Axial Strain	Poisson
Units	[KN]	[m/m]	[m/m]	
Thin Al 4	49.75	0.0054954	-0.0018943	0.33
Thin Al 5	50.24	0.0046754	-0.0015527	0.36
Thin Al 6	51.94	0.004829	-0.001811	0.39
Average	50.64333	0.00499993	-0.0017527	0.36

2.   Calculation of Friction Coefficient and Burst Pressure

Prior to using the test device for determining the properties of an unknown material, the coefficient of friction between the ram and wedges must be determined. Equations 1 and 2 were solved for the friction coefficient as shown in Equations 3 and 4 for thin and thick cylinder assumptions, respectively. Using the known Young's Modulus of the 6061 T6 aluminum along with the machine force at a measured hoop strain of 0.002 corresponding to the end of the elastic region, an experimental friction coefficient was found for thick and thin cylinders.

$$\mu = \frac{F\tan\theta - \varepsilon\pi ELt}{\varepsilon\pi ELt\tan\theta + F} \tag{3}$$

$$\mu = \frac{2a^2 F\tan\theta - \pi RLE(b^2 - a^2)\varepsilon_\theta}{\pi RLE(b^2 - a^2)\varepsilon_\theta \tan\theta + 2a^2 F} \tag{4}$$

The MATLAB script in Appendix A was used to solve for a thin and thick cylinder friction coefficient using the experimental data as explained above. The values determined by averaging the results from each strain gage on thin aluminum cylinders #4 through #6 are shown in Table 6. Since the thin aluminum cylinder meets the requirements to use thin cylinder assumptions, the friction coefficients calculated using both thin and thick cylinder equations are similar. The calculated friction coefficients show variation by just under a factor of two between runs and this is likely due to differences in lubrication between trials. The average coefficient of friction calculated with thick cylinder equations of 0.12 will be used for all future calculations.

45

Table 6.   Experimentally Determined Friction Coefficients Using Thin and
Thick Cylinder Assumptions.

Run	4	5	6	Average
mu thin cyl equations	0.09	0.17	0.13	0.13
mu thick cyl equations	0.08	0.15	0.12	0.12

As a further verification of both the finite element model and the experimentally determined friction coefficient, the averaged results from thin aluminum cylinders 4 through 6 were plotted along with the ANSYS model results with friction set to 0.12 to match the experimental value in Figure 43. The experimental and finite element results for the 0.12 friction coefficient match well in the elastic region. Above that point, the finite element model over-estimates the required force for a given hoop strain. This difference was attributed to the constant linear strain hardening model used for the FEA vice the non-linear response of experimental cylinders. This is supported by the good correlation between the experimental and finite element results in the elastic region.
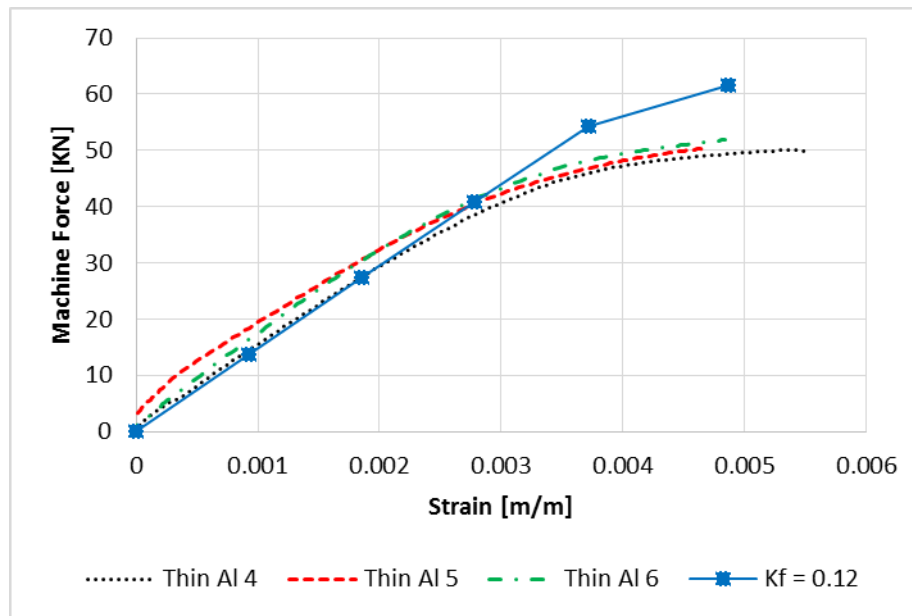
Figure 43.   Averaged Results for Thin Aluminum 4–6 and Finite Element Model
for Friction Coefficient Equal to 0.12.

As a final comparison, the observed burst pressures for thin aluminum cylinders #4 through #6 were compared to the burst pressure predicted by the finite element model as well as an analytic model based on the internal pressure recorded at an external cylinder hoop strain of 0.002 corresponding to the assumed yield point. The FEA models were computed at intervals of target hoop strains resulting in a small failure range vice a specific point. The finite element model predicted failure between hoop strains of 0.04 and 0.05 so the machine force at those strains was averaged in the calculations. Equation 5 [16] was used to determine the fully plastic (burst) pressure from the pressure at yield.

$$P_P = P_Y \frac{2b^2}{b^2 - a^2} \ln \frac{b}{a} \qquad (5)$$

The experimental, analytic, and finite element model burst pressures are summarized in Table 7. The analytic burst pressures underestimate the observed burst pressures by an average of approximately 27%. Equation 6 used to calculate the analytic burst pressure assumed a perfectly plastic material without strain hardening and this accounts for the lower burst pressures found using the analytic method. The finite element model overestimates the burst pressure by an average of approximately 24%. The FEA used a linear-plastic model with constant strain hardening using the system default value for aluminum alloys in ANSYS. Differences between this assumption and the truly nonlinear response of the test cylinders account for the difference. Interestingly, averaging the burst pressures from the analytic and finite element methods give a result near the observed burst pressures in each test run.

Table 7.   Experimental, Analytic and Finite Element Burst Pressures for Thin Aluminum Cylinders.

Run	4	5	6	Average
Obs. Burst P [Pa]	1.81E+07	1.82E+07	1.88E+07	1.84E+07
Analytic Burst P [Pa]	1.17E+07	1.50E+07	1.35E+07	1.34E+07
Error	-35.41%	-17.65%	-28.41%	-27.15%
ANSYS Burst P [Pa]	2.27E+07			
Error P [Pa]	25.89%	24.69%	20.61%	23.69%

B. THICK ALUMINUM CYLINDER

Thick aluminum #1 was tested to the limit of the test device without failing. The machine force vs strain results are shown in Figure 44. While 4 uniaxial strain gages were connected for this test, two of the solder joints broke during the test and their results were discarded. The two functioning channels showed excellent correlation throughout the duration of the test. A clear transition from linear elastic to non-linear behavior is observable at 0.002 hoop strain as expected for aluminum. While these results support validation of the test device, larger hoop strains with significant plastic deformation allow for more non-uniformities as the device expands. Additionally, while the finite element model predicted significant variation in hoop strain with location relative to a wedge, the two functioning channels for thin aluminum 1 were both centered on a wedge so it was not possible to validate that prediction for the thick cylinder. Due to the inability of the test device to provide sufficient expansion for failure of the thick cylinder and the risk of getting the test device stuck inside the test cylinder, thick aluminum #2 was not tested.
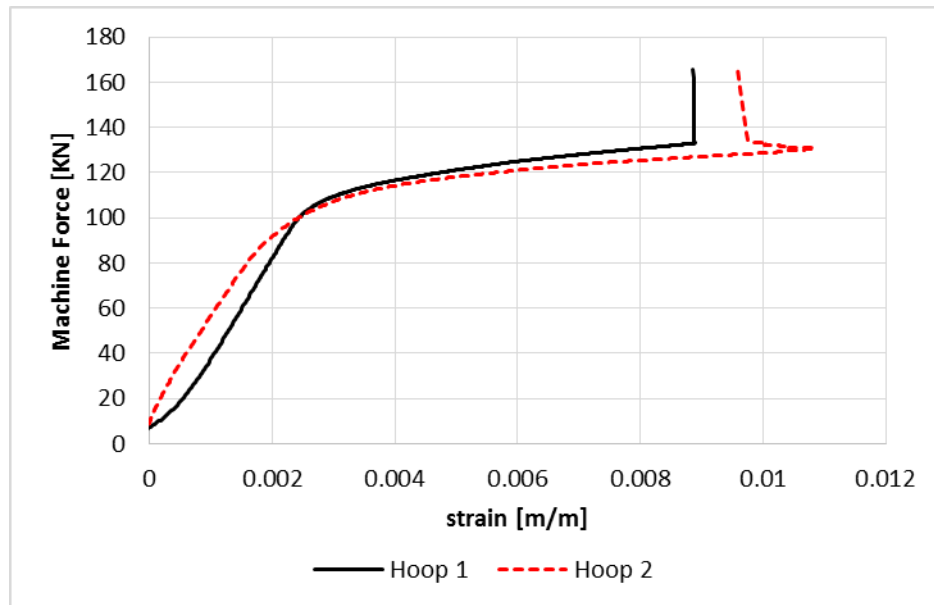
Figure 44.   Thick Aluminum #1 Test Results.

C. GLASS FIBER COMPOSITE CYLINDER

Three GFC cylinders were fabricated and strain gages were attached in preparation for experimental testing. All three were successfully tested to failure with valid data logging. Results from the testing are discussed below.

1. Results

GFC #1 was successfully tested to failure and the results are shown in Figure 45. The good correlation between the three hoop channels is attributed to good alignment of the GFC strands during fabrication, good alignment of the strain gages in the hoop and axial direction, and good alignment of strain gages to individual strands of the composite material. Channel 1 was centered on a wedge recorded the highest strain throughout the test as expected based on the finite element analysis performed for the aluminum cylinders. Channel 3 was centered on a gap and recorded the lowest strain during the test as expected. The force versus strain response was essentially linear all the way to failure indicating a brittle material consistent with GFC. The recorded hoop strain at failure was between 0.01 and 0.015 with a machine force of just under 60 kN. Averaging the three hoop channels and single functioning axial channel allowed for calculating a Poisson's ratio of 0.19.
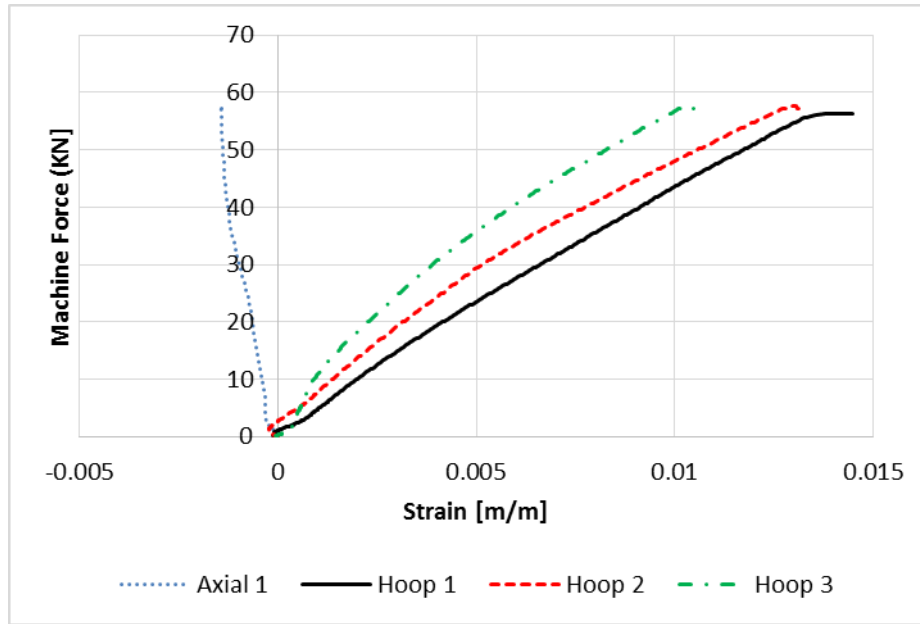
Figure 45.　7Glass Fiber Composite #1 Test Results.

The failure location of GFC #1 is shown in Figure 46. The failure is primarily axial and aligned with the axial strands of the GFC weave. While the actual rupture location is relatively clean, there was significant delamination of the composite on either side of the failure line with a minimum near the midlength of the cylinder and becoming larger at the top and bottom of the cylinder.

Figure 46.　Glass Fiber Composite #1 Failure Location.

GFC #2 was successfully tested to failure and the results are shown in Figure 47. As with GFC #1, there is good correlation in the data from all four strain gages. Again, the data shows an essentially linear response through failure which is expected for a brittle material. Furthermore, the machine force at failure is well matched with that observed during the test of GFC #1 at just over 60 kN. Failure strain was also consistent at values near 0.015 for all channels.
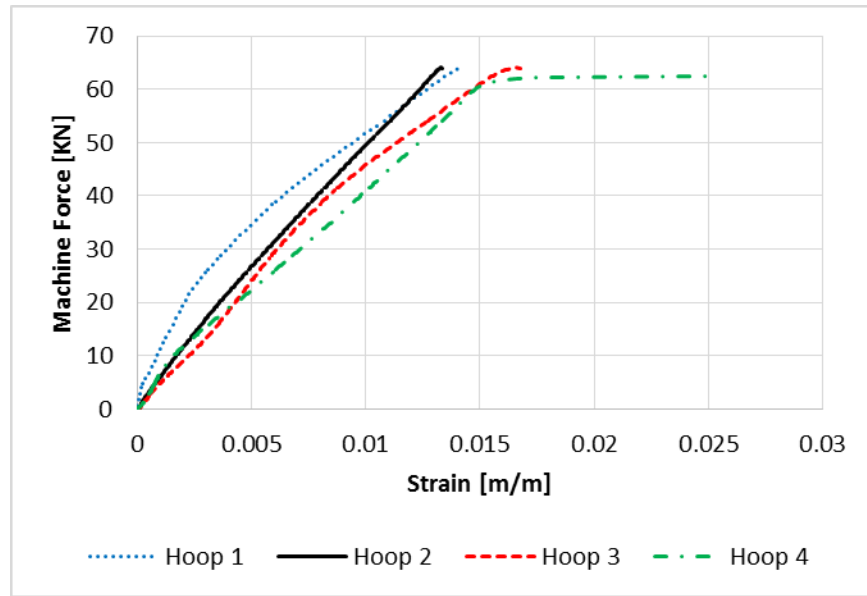
Figure 47.   Glass Fiber Composite #2 Test Results.

The failure location of GFC #2 is shown in Figure 48. Unlike GFC #1, the rupture is not purely in the axial location and shows a discontinuity at the midlength of the cylinder. Below the midlength, the failure is axial while above the midlength, the rupture was tripped and began spreading in the hoop dirction with a gradual return to the axial direction at the top of the cylinder. Based on the sharp angle of the discontinuity, there was something internal to the cylinder causing the discontinuity. Visual inspection of the failed cylinder fdid not show an obvious cause. However, it is likely that something during the fabrication process was the proximate cause of the unexpected failure appearance.

Figure 48.   Glass Fiber Composite #2 Failure Location.

GFC #3 was successfully tested to failure and the results are shown in Figure 49. The failure force of approximately 60 kN correlates well with the previous GFC cylinders although there is more significant spread in the recorded hoop strains than previously seen. While the results were still linear to failure, the variation between channels was not expected for a brittle material. Furthermore, the two axial strain channels showed positive strain throughout the test and axial channel 1 recorded a nonlinear response with increasing then decreasing axial strains. The unexpected results were determined to be the result of poor alignment of strain gages both on the hoop axis and to individual composite strands. The channel 1 rosette was off axis by approximately 10 degrees as well as being poorly aligned with an axial strand leading to the results observed on channel 1. Channel 2 was poorly aligned with an axial strand and channel 3 was poorly aligned with a hoop strand resulting in the unexpected positive axial strain in channel 2 and the lower-than-expected hoop strain in channel 3.
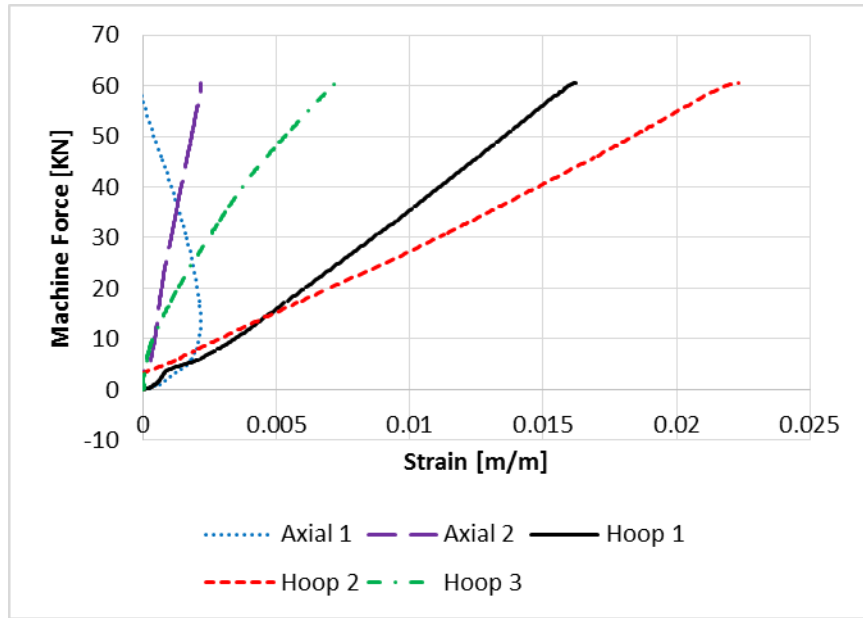
Figure 49.   Glass Fiber Composite #3 Test Results.

The failure location of GFC #3 is shown in Figure 50 and appears very similar to the failure location of GFC #1. The failure line is essentially axial with delamination spreading in the circumferential direction as the rupture approaches either end of the cylinder. Examination of high speed video showed that the failure initiates near the cylinder midlength and spreads to either end as shown in the screenshot in Figure 51. The rupture initation at midlength and spreading to either end is the likely cause of the wider delaminated areas seen at the ends of GFC #1 and #3 compared to midlength. Furthermore, the failure was observed to initiate internal to the cylinder as expected due to to maximum hoop stress being present at the inner surface.

Figure 50.   Glass Fiber Composite #3 Failure Location.
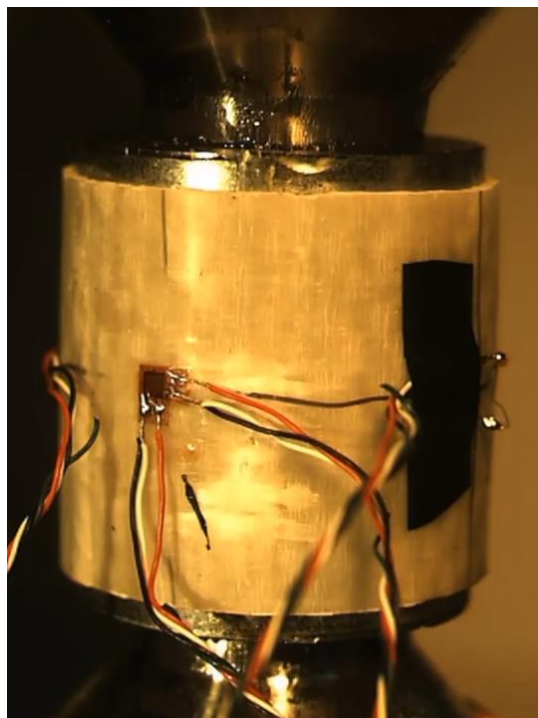
Figure 51.   Screen Shot of High Speed Video Taken at 750 Frames per Second.

To check for repeatability among the results of all three GFC cylinders tested, their average machine force and hoop strains were plotted in Figure 52. Even with the abnormalities observed in GFC #3 due to strain gage alignment, when averaged, the results for all GFC cylinders are consistent. Due to this repeatability, the results of GFC #1 through #3 were used to determine the elastic modulus of the GFC cylinder as described in the following section.
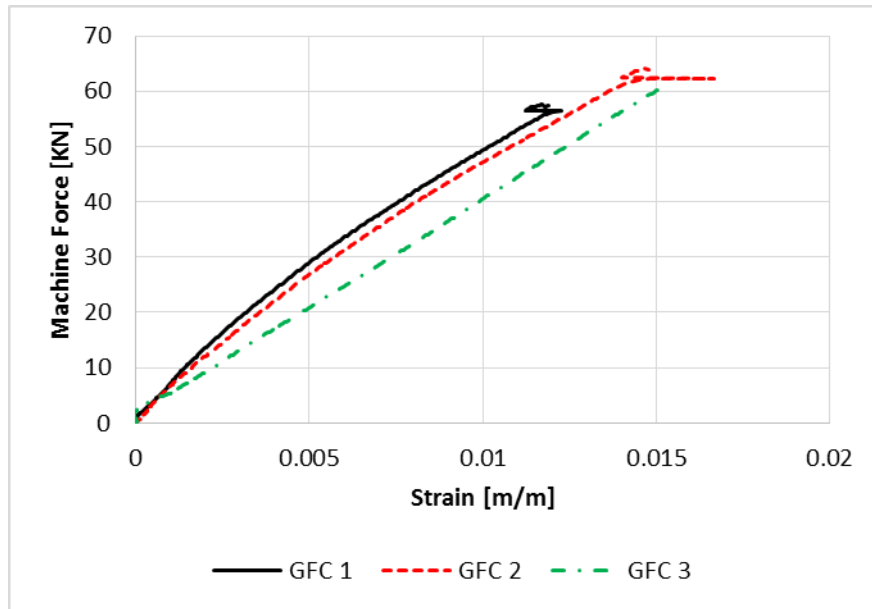
Figure 52.   Averaged Results from GFC 1, 2, and 3

2.   Elastic Modulus and Burst Pressure

To determine the elastic modulus from experimental data, Equation 2 was solved for "E" as shown in Equation 6. The strain, machine force, and angle are known values and the friction coefficient was 0.12 as determined by previous tests with thin aluminum cylinders #4 through #6. Additionally, an equation for the internal pressure applied to the test cylinder was derived using the free body diagrams in Figure 15 and Figure 16, resulting in Equation 7.

$$E = \frac{2a^2 F}{\pi RLE(b^2 - a^{2)}} \frac{\tan\theta - \mu}{1 + \mu\tan\theta} \qquad (6)$$

(3)

$$P = \frac{F}{\pi RL} \cdot \frac{\tan\theta - \mu}{1 + \mu\tan\theta} \qquad (7)$$

The MATLAB script in appendix A was created to perform the calculations in Equations 7 and 8 quickly with the results summarized in Table 8. Burst pressure was determined to be between 10.4 and 11.6 MPa with an average of 11.1 MPa. Since Equation 8 does not utilize strain measurements, these calculations are not affected by the poor strain gage alignment of GFC #2 and show good correlation. The calculated Young's modulus shows somewhat more variation with values ranging from 16 GPa to 20.2 GPa. This larger variation is due to the calculations using measured strain values which were influenced on GFC #2 by poor strain gage alignment. Removing the Young's modulus determined from GFC #2 data reduced the variation by a factor of two.

Table 8.   Glass Fiber Composite Calculated Young's Modulus and Burst Pressure.

Run	1	2	3	Average
Force [KN]	57.41	63.82	60.61	60.61
Obs. Burst P [Pa]	1.04E+07	1.16E+07	1.10E+07	1.10E+07
E Cylinder [Pa]	1.91E+10	1.64E+10	2.06E+10	1.87E+10

D.   CARBON FIBER COMPOSITE

Four CFC cylinders were fabricated and prepared for testing by attaching strain gages. Valid data was obtained during the testing of each CFC to failure and the results are detailed below.

1.   Cylinder Results

CFC #1 was successfully tested to failure and the results are shown in Figure 53. One of the four uniaxial strain gages attached to the cylinder became detached during the

test and its measurements are not included. The hoop strain measured by the three functioning channels varied significantly in both magnitude and slope. Contrary to expectations for a brittle material such as CFC, the measured hoop strain was not primarily linear. Furthermore, hoop channel 3 showed an initial negative hoop strain until the applied machine force exceeded 25 kN. Examination of the cylinder and strain gages following the test revealed that while all gages were aligned to a composite strand, they were attached off the hoop axis by 5–10 degrees. Additionally, the axial composite strands of the cylinder were tilted by as much as 10 degrees throughout the thickness of the cylinder. These two effects combined were determined to be the cause of the nonlinear strain response as well as the negative hoop strain recorded on channel 3.

Figure 53.   Carbon Fiber Composite #1 Test Results.

The failure location for CFC #1 is shown in Figure 54 and is in the axial direction as expected. The rupture line was very clean with no observable delamination or spreading throughout the length of the cylinder. Obervation of the cylinder prior to testing revealed an axial defect running the length of the cylinder from the final step of the fabrication process. This failure line followed this defect since it provided a stress concentration point to assist in initiating failure.

Figure 54.   Carbon Fiber Composite #1 Failure Location.

CFC #2 was successfully tested to failure and the results are plotted in Figure 55. Hoop channels 2 and 3 showed good correlation with similar force-strain response throughout the duration of the test. Hoop channel 1 recorded an unexpected negative hoop strain below a machine force of approximately 10 kN while the corresponding axial strain channel recorded an unexpected positive strain below approximately 25 kN. Post-test inspection of the cylinder showed that the stain gage rosette for channel one overlapped two composite hoop and axial strands. Additionally, the axial strands of the cylinder were tilted by as much as 10 degrees on the outer surface of the cylinder. As with CFC #1, it was determined that these two effects directly resulted in the strange behavior recorded by hoop and axial channel 1. Channels 2 and 3 gages were correctly aligned and their results were linear as expected for the brittle CFC cylinder. Finally, the as-expected axial strain recorded by axial channel 2 was used with the averaged hoop strains from channel 2 and 3 to calculate a Poisson's ratio of 0.15.

Figure 55.   Carbon Fiber Composite #2 Test Results.

The failure location of CFC #2 is shown in Figure 56. The rupture line was in the axial direction as expected and shows a less-clean failure than was observed with CFC #1. Inspection of the test cylinder prior to testing revealed an axial defect in the outer surface created during the fabrication process. The defect was less severe than that observed in CFC #1. However, as the failure line again corresponded to the defect location, it was determined to be a sufficient stress concentrator to initiate failure.

Figure 56.   Carbon Fiber Composite #2 Failure Location.

59

CFC #3 was successfully tested to failure and the results are shown in Figure 57. The measured response from all channels was well-correlated and linear as expected for the brittle CFC cylinder. Post-test observation showed that unlike the previous CFC cylinders, all channels were well-aligned in the hoop and axial directions as well as being centered on composite strands. Furthermore, while axial composite strains showed some tilting on the inner layers of the cylinder, they were well-aligned on the outer layer. The correct alignment and improved fabrication made possible the better results seen with CFC #3.

Hoop channel 1 measured a lower strain during the majority of the test run and was centered on a gap. This result was predicted by finite element analysis and observed in testing of the thin aluminum and GFC cylinders. Hoop channels 2 and 3 were both centered on wedges so their overlapping results were also expected. The axial and hoop strains were averaged to determine a Poisson's ratio of 0.09.
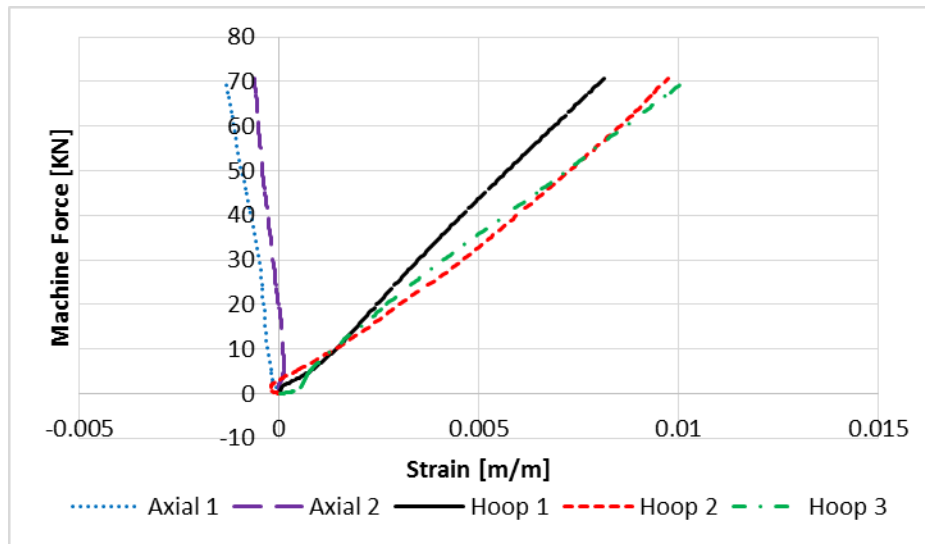
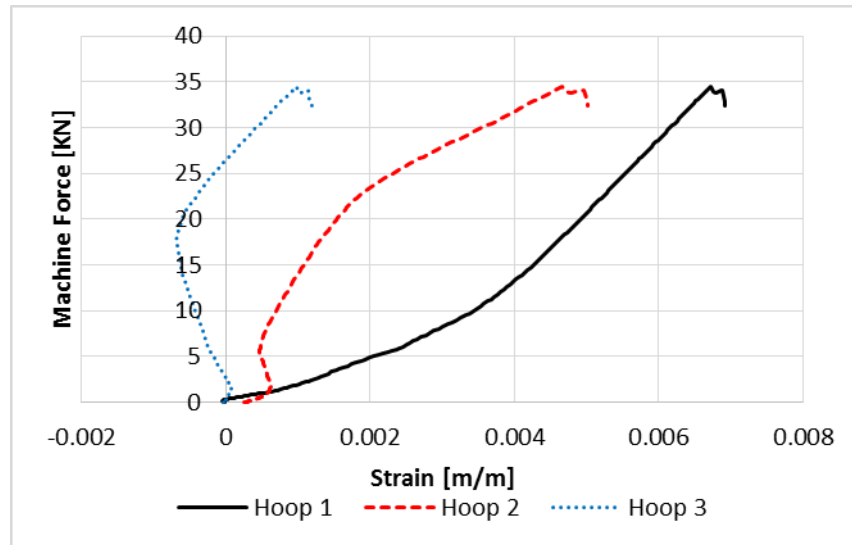Figure 57.   Carbon Fiber Composite #3 Test Results.

The failure location of CFC #3 is shown in Figure 58 and is primarily in the axial direction with some tilting. The tilting was observed to correspond with the off-axis tilting of the CFC strands on the inner layer of the cylinder. Additionally, the failure was not as clean and the previously tested CFC cylinders. Pre-test inspection of CFC #3

showed no axial defect as was observed on CFC #1 and #2. The lack of a major axial defect along with the improved alignment of axial strands allowed for the higher 70 kN machine force at failure compared to the 35 kN and 50 kN observed during testing of CFC #1 and #2.

Figure 58.   Carbon Fiber Composite #3 Failure Location.

CFC #4 was successfully tested to failure and the results are plotted in Figure 59. Hoop channels 2 and 3 are well-matched while the hoop strain recorded by channel 1 is approximately three times higher throughout the test. Variations in wall thickness by as much as 0.5 mm along with fabrication defects such as voids and were determined to be the cause of the large variation. All channels show a linear response as expected for a brittle material. Conversely, both axial channels were non-linear with axial channel 1 showing a positive strain above 30 kN machine force. Also contrary to expectations, axial channel 2 measured a positive hoop strain below approximately 30 kN machine force. Inspection of CFC #4 following the test revealed the axial strands of the cylinder were tilted by as much as 15 degrees throughout the wall thickness. This fabrication flaw was determined to be the cause of the unexpected observed axial strains. Hoop channel 1 showed good alignment in the hoop direction and was properly aligned with a hoop

composite strand while hoop channels 2 and 3 had overlap with two separate hoop strands. The CFC #4 failure hoop strain recorded by channel 1 checks with the failure hoop strains observed for CFC #3. For this reason, the variation in hoop strains for CFC #4 was determined to be caused by the overlap of composite strands in hoop channels 2 and 3.

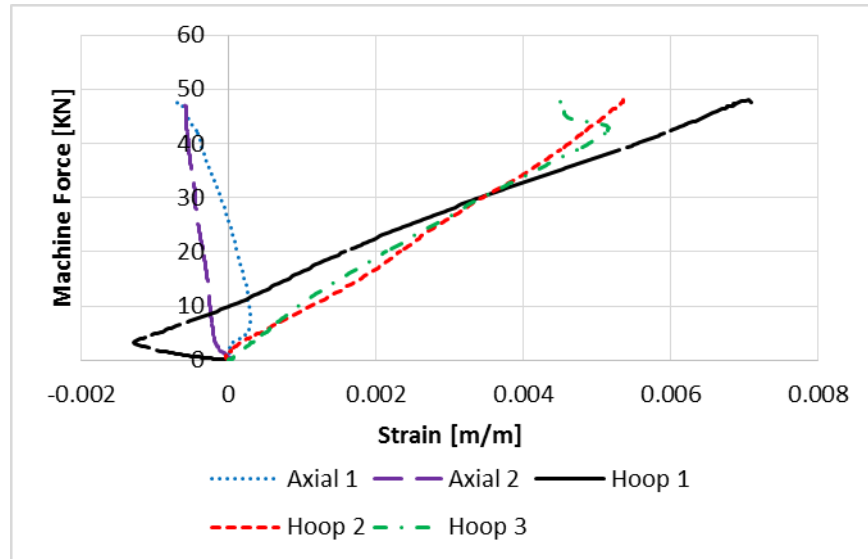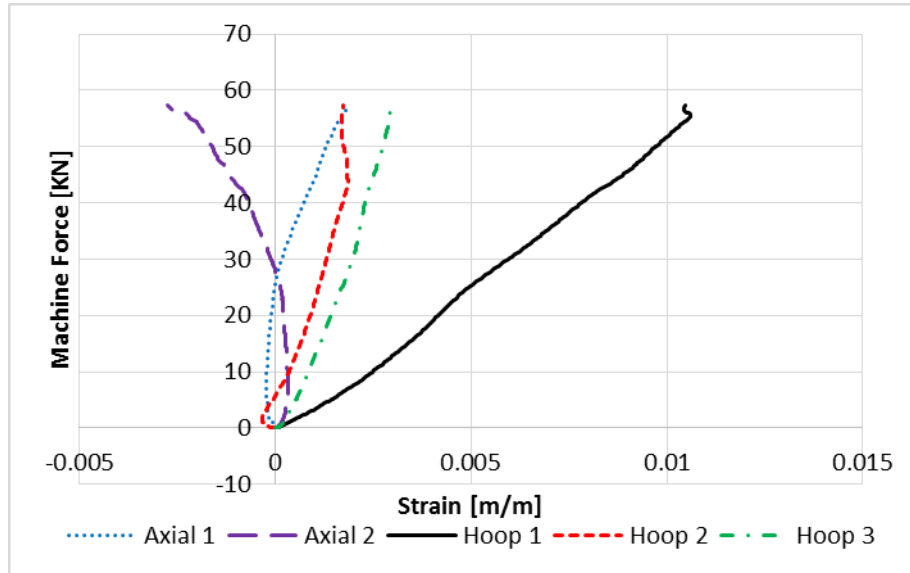Figure 59.   Carbon Fiber Composite #4 Test Results.

The failure location of CFC #4 is shown in Figure 60. The failure line aligned with the tilted axial strands. A small surface defect from the fabrication process corresponds to the failure line at the bottom of the cylinder indicating the initation point of rupture. Unlike CFC #1 and #2, the failure line does not follow the defect line through the length of the cylinder.

Figure 60.   Carbon Fiber Composite #4 Failure Location.

To check for repeatability and validate the results prior to performing calculations to determine the elastic modulus of the CFC cylinders, the hoop strain results from each CFC cylinder test were averaged and plotted in Figure 61. Even though the hoop strains from CFC #1, #2, and #4 showed more variation that was recorded for CFC #3, the averaged results are similar in slope. Although the machine force and hoop strain at failure shows variation, the slope of the force-strain curve for each test run are similar. The relationship between machine force and hoop strain is used in Equation 7 to determine the Young's modulus and the similarity in this relationship between all CFC cylinder tests indicate they can be trusted for the calculation. The variation in failure strength was determined to be caused primarily by surface defects from the manufacturing process. CFC #1, #2, and #4 all had this defect to a degree and showed a lower machine force at failure than CFC #3, which had no significant surface defects. The variation in hoop strain at failure was again due to the presence of surface defects in CFC #1, #2, and #4 as well as poor alignment of several strain gages as discussed in the individual cylinder results above.
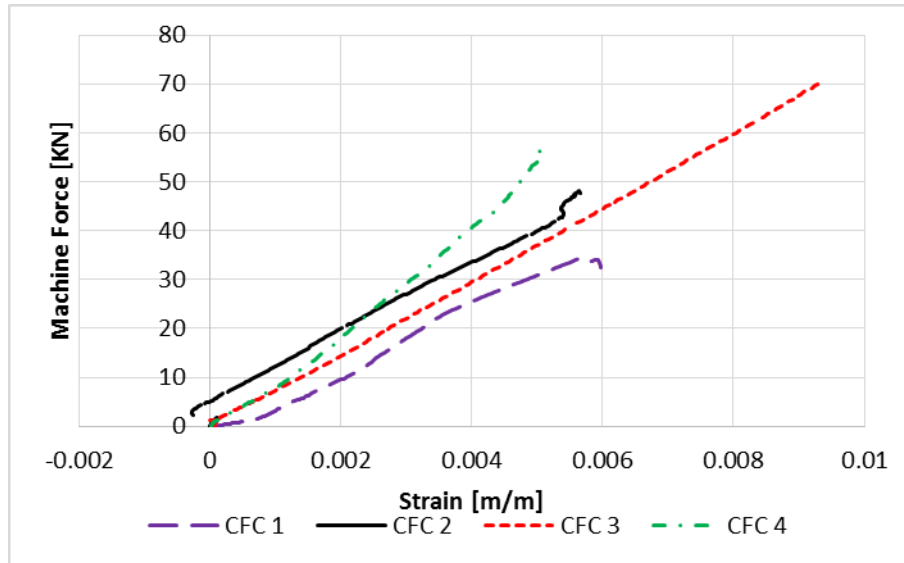
Figure 61.   Carbon Fiber Composite 1–4 Averaged Results.

2.   Tensile Specimen Results

To provide a reliable check of the elastic modulus to be determined from the cylinder test device results, three CFC tensile specimens were tested to failure. Data from the third specimen was corrupted and is not included in this analysis. The force versus strain results from the tests are shown in Figure 62 and exhibit linear response through failure as expected for brittle materials. The machine force at failure is well-matched between the two runs although test 2 showed somewhat larger longitudinal and transverse strains at failure. The variation in results was attributed to alignment of the strain gage rosettes to the axial and transverse strands of the tensile specimens. Small overlaps of both strands were observed to varying levels in all tensile specimens. Using averaged results from the hoop and axial strain gages, the Poisson's ratio was found to be 0.16.
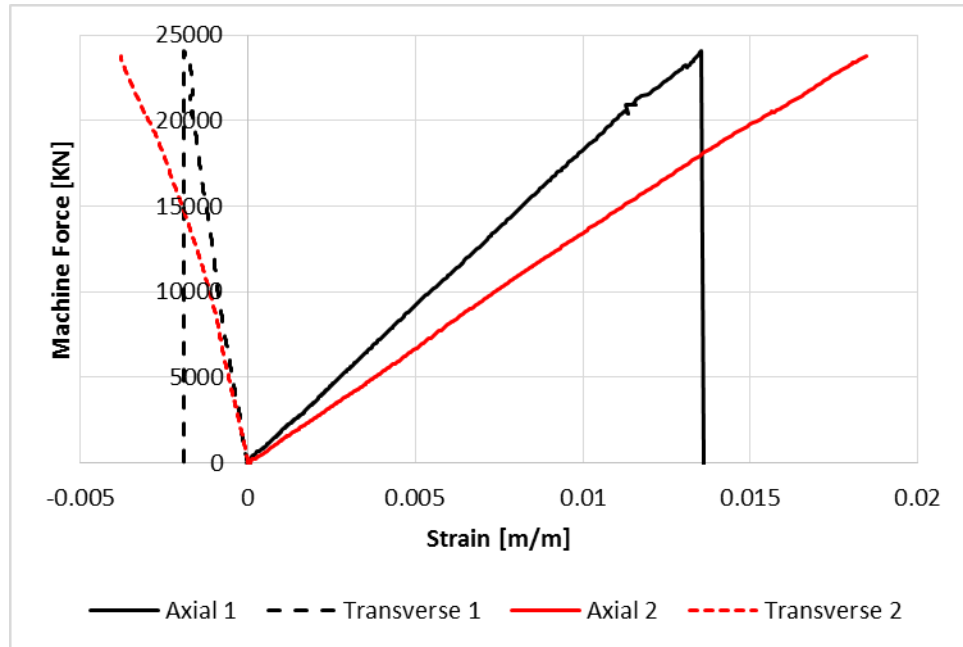
Figure 62.   Carbon Fiber Composite Tensile Test Results.

The tensile specimens after testing are shown in Figure 63. All failures are simlar in appearance and show little delamination..

Figure 63.   Tensile Specimens after Testing.

3. Elastic Modulus and Burst Pressure

As with the GFC cylinders, the elastic modulus of the CFC cylinders was determined using Equation 7 with the machine force and strain values measured during testing of CFC #1 through CFC #4. The friction coefficient of 0.12 determined from the thin aluminum cylinder tests was used as with the GFC calculations. The burst pressure for each was similarly determined using Equation 8.

To determine the elastic modulus of the CFC tensile specimens, the area of the gage section was used to determine the axial stress from the machine force recorded during the tests. The stress-strain curves were then plotted in Figure 64 and a linear trend line used to determine the elastic modulus. The variation between the two cylinders was attributed to difference in the amount and alignment of longitudinal composite strands relative to the gage section of the specimen.
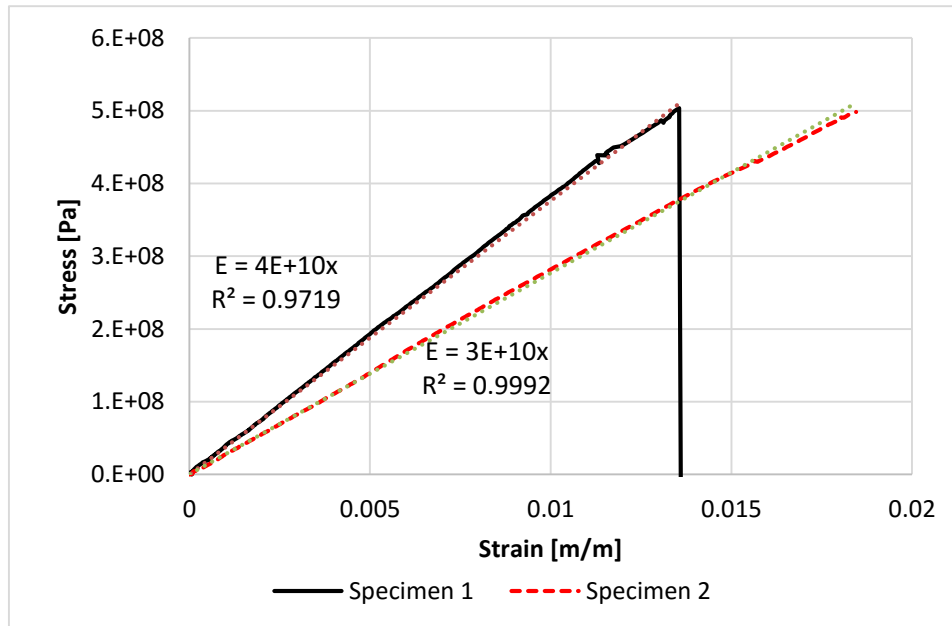
Figure 64.   Tensile Specimen Stress-Strain Curves.

The tabulated results from the CFC cylinder and tensile specimen are shown in Table 9. The observed burst pressure shows significant variation between test runs and

was expected due to the variation in machine force at failure. The variation was previously determined to be primarily due to axial surface defects created during the fabrication process. The average elastic modulus derived from the cylinder testing was 51.1 GPa compared to an average of 35 GPa from the tensile specimens, a relative error of 46%. Of the CFC cylinders tested, only CFC 3 had overlapping data from all hoop strain channels as well as no significant surface defect. Comparing the elastic modulus of CFC #3 to the average from the tensile tests results in a smaller relative error of 9.4%.

Table 9.   Carbon Fiber Composite Calculated Young's Modulus and Burst Pressure.

Run	1	2	3	4	Average
Force [kN]	32.42	48.05	70.64	57.27	52.095
Obs. Burst P [Pa]	5.88E+06	8.40E+06	1.28E+07	1.04E+07	9.37E+06
E Cylinder [Pa]	2.69E+10	4.04E+10	3.67E+10	9.35E+10	4.94E+10
E Tensile [Pa]	4.00E+10	3.00E+10	No data		3.50E+10

E.   SUMMARY OF RESULTS

After validation of the cylinder test device functionality the experimental testing had two primary purposes. First, the machine force and hoop strains recorded during several thin aluminum cylinders were used to calculate the friction coefficient of the test device. With the coefficient of friction between the ram and wedges known, the measured force and hoop strains for the remaining cylinder tests could be used to determine the burst pressure and elastic modulus of the composite cylinder. Additionally, runs with valid axial and hoop strain data were used to determine the Poisson's ratio of the cylinder material. To validate the CFC cylinder results, data from two CFC tensile specimens were also used to provide a second means of determining the elastic modulus and Poisson's ratio of the CFC.

The combined experimental and analysis results for all runs with data used in calculations and analysis are shown in Table 10. Adequate repeatability was an important factor during the testing and an effort was made to collect data for a sufficient number of

tests to show sufficient repeatability. Since the experimentally determined friction coefficient is used in all calculations for burst pressure and Young's modulus, its accurate determination was vital. Three thin aluminum trials 4 through 6 were used and while the calculated friction coefficient varied from 0.08 to 0.15, the three data sets were determined to be sufficient for averaging for a final value of 0.12. Additional tests of cylinders with known properties would be useful for better determination of the variability of the coefficient of friction between test runs.

Determination of the elastic modulus and burst pressure of a composite cylinder were the primary motivations for this research. The GFC cylinders showed good repeatability with moduli ranging from 16.04 to 20.18 GPa. The GFC cylinders did not present any significant strand alignment issues or other fabrication defects so the variation was attributed to alignment errors on individual strain gages as discussed previously.

Due to strain gage alignment issues with GFC #3 and failure of an axial channel during GFC 1, there was only one valid axial strain data set available for computation of the Poisson's ratio of the GFC cylinders. The Poisson's ratio was determined to be 0.19 using the averaged hoop strains and single axial strain recorded for GFC. Additional GFC cylinder tests and GFC tensile tests would be useful for validating this result.

The experimental burst pressure for the three GFC cylinders showed good correlation as expected based on the similar machine force at failure. Burst pressures ranged from 10.42 to 11.58 MPa with an average of 11 MPa. The burst pressure calculations show less variation than seen with the GFC elastic moduli since they use only the machine force at rupture and errors introduced due to strain gage alignment do not affect the result.

The Young's moduli determined from the CFC cylinder tests in Table 9 showed significantly more variation than was observed with the GFC cylinders with values ranging from 28.08 to 97.58 GPa. This variation resulted in a higher test device-determined modulus of elasticity of 51.08 GPa compared to the average 35 GPa calculated from the CFC tensile tests, an error of nearly 46%. Inspection of the CFC cylinders revealed strain gage alignment issues and axial surface defects of CFC #1, #2,

and #4 as well as varying levels of axial composite strand tilting on all CFC cylinders. These effects directly resulted in the large variation in results for the four CFC cylinders. CFC #3 had no significant surface defect and better strain gauge alignment. The elastic modulus of CFC #3 of 38.26 GPa compares more favorably to the average 35 GPa calculated from the tensile tests with a relative error of 9.3%.

The Poisson's ratio of the CFC was determined using data from CFC #2, CFC #3, and the two CFC tensile specimens. As with the Young's Modulus, the CFC cylinder Poisson's ratio showed a relatively large variation ranging from 0.089 to 0.15 while the tensile specimens were more consistent ranging from 0.158 to 0.166. As before, the large variation in the CFC cylinder results was likely due to axial strand errors during fabrication as well as strain gage alignment problems.

The experimental burst pressure for all four CFC cylinders showed significant variation, ranging from 5.88 to 12.82 MPa. This is primarily due to the presence of axial surface defects on CFC #1, #2, and #4 acting as stress concentrators and initiating early rupture. CFC #3 had no significant axial surface defect and presented the highest rupture pressure supporting this argument.

Table 10.   Experimental and Analysis Result Summary.

Run	mu	E [GPa]	Poisson	Experimental Burst Pressure [MPa]	Finite Element Burst Pressure [MPa]	Analytic Burst Pressure [MPa]
Thin Al 4	0.08		0.33	18.06	11.66	
Thin Al 5	0.15		0.36	18.23	15.01	22.7
Thin Al 6	0.12		0.39	18.84	13.49	
Thin Al avg	0.12		0.36	18.38	13.39	
GFC 1		19.12	0.19	10.42		
GFC 2		16.35		11.58		
GFC 3		20.58		10.99		
GFC avg		18.68		11.00		
CFC 1		26.91		5.88		
CFC 2		40.36	0.15	8.4		
CFC 3		36.68	0.089	12.82		
CFC 4		93.53		10.39		
CFC avg		49.37	0.12	9.37		
CFC T1		40	0.166			
CFC T2		30	0.158			
CFC T avg		35	0.162			

The experimental results from this research showed that the proper alignment of strain gages are critical to achieving accurate and reliable results during a test. The strain gages must be correctly aligned in the hoop and axial direction as well as centered on a single composite strand for accurate and repeatable results. Furthermore, fabrication defects resulting in twisting of axial composite strands as was seen in the CFC cylinders results in a "virtual" misalignment of the axial strain gages and preventing the collection of valid data.

V. CONCLUSIONS, RECOMMENDATIONS AND FUTURE WORK

A. CONCLUSIONS AND RECOMMENDATIONS

During this research, a purely mechanical device capable of applying an internal pressure to an open-ended cylinder was designed, fabricated, and tested. FEA was performed prior to fabrication to validate the design and was later used for comparison to analytic and experimental results. Following validation, a test procedure was created to allow determination of the cylinder's burst pressure, elastic modulus, and Poisson's ratio.

Several thin aluminum cylinders were tested first to determine the friction coefficient of the device and to provide a comparison to FEA and analytical models with good results. GFC and CFC cylinders were then tested to determine their unknown properties. Finally, CFC tensile specimens were tested to failure to allow for comparison of the elastic modulus and Poisson's ratio determined from the test cylinders.

During the testing, it was discovered that the composite cylinder results were highly dependent on the alignment of the composite strands to the axial and hoop directions of the cylinder. Ensuring the strain gages were aligned to a single axial and hoop strand was also of great importance for valid results. Any deviation from ideal alignment inserted large errors resulting in either unexpected positive axial strains or non-linear responses. To minimize errors in future testing, greater care should be taken during the fabrication and preparation steps to ensure that the strands making up the cylinder are properly aligned both geometrically. Prior to strain gage attachment, the cylinders should be marked in the hoop and axial directions to ensure proper alignment.

This work is a vital step in fabrication CFC cylinders for dynamic testing by LLNL that have comparable properties to the steel cases to be used in the finished ADP. The test device provides a means of quickly testing cylinders at low-cost providing economical experimentation prior to the more costly instrumented dynamic testing performed by the EMC at LLNL.

B.   FUTURE WORK

During this research, valid data for calculations was collected from three thin aluminum cylinders, three GFC cylinders, four CFC cylinders, and two CFC tensile specimens. The aluminum and GFC cylinders as well as the CFC tensile specimens showed good correlation. Due to fabrication defects and strain gage alignment problems, the four CFC cylinders showed significant variation in test results. While the current data set is sufficient for a proof of concept, additional testing of CFC cylinders with the same test parameters would be useful. Additionally, future tests could be run with CFC cylinders fabricated with carbon nanotubes mixed in with the epoxy to determine the effect of alterations to the epoxy formulation.

All tests during this research were performed at a quasi-static extension rate of 2 mm/min. Conducting tests at higher extension rates would be useful for comparison with these results. Since determining the properties of the CFC cylinders used by LLNL during explosive testing is desired, differences between the static and dynamic results are important and tests at higher extension rates would help to better estimate the dynamic properties of the CFC cylinders.

All composite cylinders tested were fabricated by hand using a continuous wrap of a composite weave. This method was selected because the same material could be easily used to fabricate composite tensile specimens for comparison to the test device-determined material properties and allow for easy variation in the fabrication process. Unfortunately, manual fabrication inserts a degree of variation in each cylinder and was this especially noticeable with the testing of the CFC cylinders. The actual test cylinders used by LLNL for energetic testing are created using a continuous filament-wound process that creates a more uniform cylinder. Due to process limitations, 7.62 cm (3 in) inside-diameter continuous fiber-wound cylinders for use with the current test device were not available. Efforts are currently in progress to fabricate a test device capable of testing the smaller 5.08 cm (2 in) CFC cylinders used by LLNL for testing.

APPENDIX A. MATLAB SCRIPT

```matlab
%% Compare thin-walled cylinder to computer model

clear all
close all
clc

E_AL=71e9;
L=3*2.54/100;
t=0.125*2.54/100;
R = 1.5*2.54/100;
a = R;    % inner radius
b = R+t; % outer radius
mu=0.01;
theta=80/90*pi/2;


target_strain = [0.001 0.002 0.003 0.004 0.005];


F = [8871.1  17765 26621 35436 39504];


% Thin Cylinder predicted strain at modeled force for target strain
strain_thin = F/(E_AL*L*t*pi)*(tan(theta)-mu)/(1+mu*tan(theta))

% Thick Cylinder predicted strain at modeled force for target strain
den = b^2-a^2;
strain_thick = 2*a^2/E_AL/den*F/pi/b/L*(tan(theta)-
mu)/(1+mu*tan(theta))

%% Determine friction factor based on thin Al experiment data and
determine internal pressure at yield
e_el = 0.002;

% Data from mechanical testing at hoop strain = 0.002 for runs 4-6
F4 = [29.9313 23.11358 36.23686]*1000;
F5 =[49.6358 29.53219 35.51614] *1000;
F6 =[17.97607 35.61633 49.47684] *1000;

% Friction coefficient with thin cylinder assumptions
mu_thin = [mean((F4.*tan(theta) - e_el*pi*E_AL*L*t)
./(e_el*pi*E_AL*L*t*tan(theta) + F4))...
    mean((F5.*tan(theta) - e_el*pi*E_AL*L*t)
./(e_el*pi*E_AL*L*t*tan(theta) + F5))...
    mean((F6.*tan(theta) - e_el*pi*E_AL*L*t)
./(e_el*pi*E_AL*L*t*tan(theta) + F6))]

mu = mean(mu_thin) %Friction factor averaged across three runs and 9
hoop strain gages

% Friction coefficient with thick cylinder equations
```

```matlab
mu_thick_comb = [mean((2*a^2*F4*tan(theta)-
pi*R*L*E_AL*den*e_el)./(pi*R*L*E_AL*den*e_el*tan(theta) + 2*a^2*F4))...
    mean((2*a^2*F5*tan(theta)-
pi*R*L*E_AL*den*e_el)./(pi*R*L*E_AL*den*e_el*tan(theta) + 2*a^2*F5))...
    mean((2*a^2*F6*tan(theta)-
pi*R*L*E_AL*den*e_el)./(pi*R*L*E_AL*den*e_el*tan(theta) + 2*a^2*F6))]

mu_thick = mean(mu_thick_comb) % Friction factor averaged across three
runs and 9 hoop strain gages

% Calculate Pi at 0.002 hoop strain
Py_AL = [mean(F4./pi/R/L.*((tan(theta)-
mu_thick)/(1+mu_thick*tan(theta))))...
    mean(F5./pi/R/L.*((tan(theta)-
mu_thick)/(1+mu_thick*tan(theta))))...
    mean(F6./pi/R/L.*((tan(theta)-mu_thick)/(1+mu_thick*tan(theta))))]

Py_Al_avg = mean(Py_AL)

%% Determine E and burst pressure for GFC cylinders

% Input data
aGFC = 3*2.54/100 % Inner radius [m]
bGFC = aGFC + 3.3/1000 % Outer radious [m]
den = bGFC^2-aGFC^2;

F_GFC1 = 57405.82;
e_GFC1 = [0.014473 0.013227 0.010604];
F_GFC2 = 63820;
e_GFC2 = [0.014178 0.013364 0.01678 0.024894];
F_GFC3 = 60606.44;
e_GFC3 = [.016215 .02232 .007293];

% Calculate Young's Modulus based on above data and assumed mu
E_GFC_thin = [mean(F_GFC1./(pi.*e_GFC1*L*t) .* (tan(theta)-
mu)/(1+mu*tan(theta)))...
    mean(F_GFC2./(pi.*e_GFC2*L*t)  .* (tan(theta)-
mu)/(1+mu*tan(theta)))...
    mean(F_GFC3./(pi.*e_GFC3*L*t)  .* (tan(theta)-
mu)/(1+mu*tan(theta)))]

E_GFC_thick = [mean(2*aGFC^2*F_GFC1./(pi*bGFC*L.*e_GFC1*den) .*
(tan(theta)-mu_thick)/(1+mu_thick*tan(theta)))...
    mean(2*aGFC^2*F_GFC2./(pi*bGFC*L.*e_GFC2*den) .* (tan(theta)-
mu_thick)/(1+mu_thick*tan(theta)))...
    mean(2*aGFC^2*F_GFC3./(pi*bGFC*L.*e_GFC3*den) .* (tan(theta)-
mu_thick)/(1+mu_thick*tan(theta)))]

% E for the two best GFC cylinders based on 7 hoop strain gages
E_GFC_thin_avg = mean(E_GFC_thin)
E_GFC_thick_avg = mean(E_GFC_thick)

% Experimental Burst Pressure
```

```matlab
P_GFC = [mean(F_GFC1./pi/aGFC/L.*((tan(theta)-
mu_thick)/(1+mu_thick*tan(theta))))...
    mean(F_GFC2./pi/aGFC/L.*((tan(theta)-
mu_thick)/(1+mu_thick*tan(theta))))...
    mean(F_GFC3./pi/aGFC/L.*((tan(theta)-
mu_thick)/(1+mu_thick*tan(theta))))]
P_GFC_avg = mean(P_GFC)

%% Determine E and burst pressure for CFC cylinders

% Input Data
aCFC = 3*2.54/100 % Inner radius [m]
bCFC = aCFC + 2.7/1000 % Outer radious [m]
den = bCFC^2-aCFC^2;; % Geometry-based constant
F_CFC1 = 32424.66;
e_CFC1 = [0.00501 0.0069175];
F_CFC2 = 48048.9;
e_CFC2 = [0.0070467 0.0053568 0.005159];
F_CFC3 = 70637.48;
e_CFC3 = [0.0081403 0.0097439   0.010259];
F_CFC4 = 57266.58;
e_CFC4 = [.010464 .001734 .00291];

% Calculate Young's Modulus based on above data and assumed mu
E_CFC_thin = [mean(F_CFC1./(pi.*e_CFC1*L*t) .* (tan(theta)-
mu)/(1+mu*tan(theta)))...
    mean(F_CFC2./(pi.*e_CFC2*L*t) .* (tan(theta)-
mu)/(1+mu*tan(theta)))...
    mean(F_CFC3./(pi.*e_CFC3*L*t) .* (tan(theta)-
mu)/(1+mu*tan(theta)))...
    mean(F_CFC4./(pi.*e_CFC4*L*t) .* (tan(theta)-
mu)/(1+mu*tan(theta)))]

E_CFC_thick = [mean(2*aGFC^2*F_CFC1./(pi*bGFC*L.*e_CFC1*den) .*
(tan(theta)-mu_thick)/(1+mu_thick*tan(theta))) ...
    mean(2*aGFC^2*F_CFC2./(pi*bGFC*L.*e_CFC2*den) .* (tan(theta)-
mu_thick)/(1+mu_thick*tan(theta)))...
    mean(2*aGFC^2*F_CFC3./(pi*bGFC*L.*e_CFC3*den) .* (tan(theta)-
mu_thick)/(1+mu_thick*tan(theta)))...
    mean(2*aGFC^2*F_CFC4./(pi*bGFC*L.*e_CFC4*den) .* (tan(theta)-
mu_thick)/(1+mu_thick*tan(theta)))]


% E for the two best CFC cylinders based on 6 hoop strain gages
E_CFC_thin_avg = mean(E_CFC_thin);
E_CFC_thick_avg = mean(E_CFC_thick);

% Eperimental Burst Pressure
P_CFC = [mean(F_CFC1./pi/aCFC/L.*((tan(theta)-
mu_thick)/(1+mu_thick*tan(theta))))...
    mean(F_CFC2./pi/aCFC/L.*((tan(theta)-
mu_thick)/(1+mu_thick*tan(theta))))...
    mean(F_CFC3./pi/aCFC/L.*((tan(theta)-
mu_thick)/(1+mu_thick*tan(theta))))...
```

```matlab
    mean(F_CFC4./pi/aCFC/L.*((tan(theta)-
mu_thick)/(1+mu_thick*tan(theta))))]


P_CFC_avg = mean(P_CFC);


%% Experimental and expected Burst Pressure for thin Aluminum cylinders
4-6
% Input Data
Fex_Al_burst = [49.75729 50.23574 51.93548]*1000;


% Experimental Burst pressure based on machine force and calculated mu
Pbex_AL_burst = Fex_Al_burst./pi/R/L.*((tan(theta)-
mu_thick)/(1+mu_thick*tan(theta)))


% Expected Burst Pressure from Borewsi et al
Pp_al = Py_AL.*2.*b^2./(b^2-a^2).*log(b/a)
Pp_al_avg = mean(Pp_al)


% Expected machine force at failure
Fp_al = Pp_al*pi*R*L*(1+mu_thick*tan(theta))/(tan(theta)-mu_thick)


% ANSY predicted burst pressure
Pbex_ANSYS = 62639/pi/R/L*((tan(theta)-
mu_thick)/(1+mu_thick*tan(theta)))
```

APPENDIX B. SUPPLEMENTARY ANSYS SETTINGS AND RESULTS

Table 11.   Baseline Results for Thin Aluminum Cylinder.

Target Strain	0	0.001	0.002	0.003	0.004	0.005	0.007
Wedge Stress	0	64.484	115.95	167.83	220.55	243.79	280.28
Wedge Strain	0	0.000329	0.000592	0.0008586	0.0011297	0.00122	0.001412
Wedge FOS	0	>15	10.406	7.1	5.47	4.9	4.3
Ram Stress	0	28.181	58.239	86.077	110.05	147.81	213.04
Ram Strain	0	0.000181	0.000311	0.0004602	0.0005933	0.00083	0.001174
Ram FOS	0	>15	>15	14	10.87	8.1	5.6
Cyl eq. Stress	0	64.141	127.85	191.57	255.5	276.11	277.09
Cyl Hoop Stress	0	64.03	127.63	191.24	254.99	279.88	281.46
Cyl eq. Strain	0	0.000931	0.001856	0.0027805	0.0037083	0.00472	0.006758
Cyl Hoop Strain	0	0.000931	0.001855	0.0027788	0.0037057	0.00402	0.00404
Cyl Axial Strain	0	-0.000307	-0.000613	-0.000918	-0.001225	-0.00121	-0.001744
Cylinder FOS	0	3.4	1.7	1.16	0.99	0.99	0.99

Table 12.   Baseline Results for Thick Aluminum Cylinder.

Target Strain	0	0.001	0.002	0.003	0.004	0.005	0.007
Wedge Stress	0	96.773	180.49	266.34	354.57	378.15	448.41
Wedge Strain	0	0.00049509	0.000925	0.001367	0.001821	0.001892	0.002264
Wedge FOS	0	12.47	6.6	4.5	3.4	3.2	2.7
Ram Stress	0	74.785	144.63	209.25	268.98	376.28	430.83
Ram Strain	0	0.0003759	0.000727	0.001052	0.001352	0.001882	0.002288
Ram FOS	0	>15	8.3	5.7	4.4	3.2	2.8
Cyl eq. Stress	0	44.563	89.053	133.56	178.09	226.56	276.33
Cyl Hoop Stress	0	44.545	89.016	133.5	178.01	226.48	279.57
Cyl eq. Strain	0	0.00064679	0.001293	0.001938	0.002585	0.003288	0.005213
Cyl Hoop Strain	0	0.00064669	0.001292	0.001938	0.002584	0.003288	0.004023
Cyl Axial Strain	0	-0.00022873	-0.00046	-0.00068	-0.00091	-0.00111	-0.0016
Cylinder FOS	0	3.9	1.9	1.3	0.97	0.99	0.99

Table 13.   Thin Cylinder Results with Friction Coefficient of 0.05.

Target Strain	0.001	0.002	0.003	0.004	0.005
Wedge Stress	64.887	116.31	168.18	220.74	244.46
Wedge Strain	0.0003309	0.000594	0.00086	0.00113	0.0012237
Ram Stress	28.592	59.273	87.677	113.21	146.54
Ram Strain	0.00018108	0.000315	0.000467	0.000603	0.0008339
Cyl eq. Stress	64.135	127.82	191.54	255.45	276.12
Cyl Hoop Stress	64.022	127.59	191.2	255.05	283.2
Cyl eq. Strain	0.00093086	0.001852	0.00278	0.003708	0.004766
Cyl Hoop Strain	0.00093028	0.001854	0.002778	0.003706	0.0040384
Al Strain	2.07793E-05	4.16E-05	6.23E-05	8.32E-05	9.2938E-05
Machine Force	10.946	21.888	32.817	43.841	48.957

Table 14.   Thin Cylinder Results with Friction Coefficient of 0.01.

Target Strain	0.001	0.002	0.003	0.004	0.005
Wedge Stress	65.507	117.14	169.25	222.33	246.39
Wedge Strain	0.00033378	0.00059777	0.0008647	0.001137	0.0012336
Ram Stress	29.672	61.428	90.891	117.11	144.59
Ram Strain	0.00018176	0.00032521	0.00048253	0.000622	0.00083312
Cyl eq. Stress	64.112	127.78	191.49	255.89	276.16
Cyl Hoop Stress	63.993	127.54	191.13	255.43	287.01
Cyl eq. Strain	0.00093052	0.0018546	0.0027792	0.003714	0.0048718
Cyl Hoop Strain	0.0009267	0.0018534	0.0027774	0.003712	0.0040529
Al Strain	2.59694E-05	5.17832E-05	7.7616E-05	0.000103	0.00011674
Machine Force	13.68	27.278	40.886	54.368	61.497

Table 15.   Thin Cylinder Results with Friction Coefficient of 0.12.

Target Strain	0.001	0.002	0.003	0.004	0.005	0.01
inner max shear	41.533	82.6	123.72	150.37	152.83	154.97
Cyl eq. Stress	64.117	127.74	191.46	255.94	276.16	278.68
Cyl Hoop Stress	63.997	127.5	191.1	255.5	288.59	293.83
Cyl eq. Strain	0.00093061	0.001854	0.002779	0.003715	0.004875	0.009874
Cyl Hoop Strain	0.00092999	0.001853	0.002777	0.003713	0.004058	0.004102
Al Strain	2.81582E-05	5.59E-05	8.39E-05	0.000112	0.000125	0.000129
Machine Force	14.833	29.469	44.213	59.185	66.093	67.967

Defaults	
Physics Preference	Mechanical
☐ Relevance	0
Sizing	
Use Advanced Size Fun...	Off
Relevance Center	Medium
☐ Element Size	Default
Initial Size Seed	Active Assembly
Smoothing	Medium
Transition	Fast
Span Angle Center	Medium
Minimum Edge Length	8.8663e-004 m
Inflation	
Use Automatic Inflation	None
Inflation Option	Smooth Transition
☐ Transition Ratio	0.272
☐ Maximum Layers	5
☐ Growth Rate	1.2
Inflation Algorithm	Pre
View Advanced Options	No
Patch Conforming Options	
Triangle Surface Mesher	Program Controlled
Patch Independent Options	
Topology Checking	Yes

Figure 65.   ANSYS Mesh Controls.

Newton-Raphson Op...	Program Controlled
Force Convergence	On
--Value	Calculated by solver
--Tolerance	2.5%
--Minimum Reference	0.1 N
Moment Convergence	Program Controlled
Displacement Conver...	Program Controlled
Rotation Convergence	Program Controlled
Line Search	Program Controlled
Stabilization	Constant
--Method	Energy
--Energy Dissipation ...	1.e-004
--Activation For First ...	No
--Stabilization Force L...	0.2

Figure 66.   ANSYS Nonlinear Controls.

Step Controls	
Number Of Steps	1.
Current Step Number	1.
Step End Time	1. s
Auto Time Stepping	Program Controlled
Solver Controls	
Solver Type	Direct
Weak Springs	On
Spring Stiffness	Factor
Spring Stiffness Factor	10
Large Deflection	On
Inertia Relief	Off

Figure 67.   ANSYS Step Controls.

LIST OF REFERENCES

[1]   Defense Threat Reduction Agency & USSSTRATCOM Center for Combating WMD & Standing Joint Force Headquarters-Elimination. (n.d.). Who we are. [Online]. Available: http://www.dtra.mil/About/WhoWeAre.aspx. Accessed Nov. 5, 2015.

[2]   Agent Defeat Weapon—NAVY/DTRA. (n.d) GlobalSecurity.org. [Online]. Available: http://www.globalsecurity.org/military/systems/munitions/adw.htm. Accessed Nov. 5, 2015

[3]   J. Molitoris, *Image courtesy of LLNL EMC,* Livermore, CA: Lawrence Livermore National Laboratory, 2015.

[4]   A. Onder, O. Sayman, T. Dogan, and N. Tarakcioglu, "Burst failure load of composite pressure vessels," *Composite Structures*, vol. 89, no. 1, pp. 159–166, Jun. 2009.

[5]   M. Xia, H. Takayanagi, and K. Kemmochi, "Analysis of multi-layered filament-wound composite pipes under internal pressure," *Composite Structures*, vol. 53, no. 4, pp. 483–491, Sep. 2001.

[6]   J. Xing, P. Geng, and T. Yang, "Stress and deformation of multiple winding angle hybrid filament-wound thick cylinder under axial loading and internal and external pressure," *Composite Structures*, vol. 131, no. 4, pp. 866–877, Nov. 2015.

[7]   T. Hwang, J. Park, and H. Kim, "Evaluation of fiber material properties in filament-wound composite pressure vessels," *Composites: Part A*, vol. 43, no. 9, pp. 1467–1475, Apr. 2012.

[8]   A. Horide, S. Wakayama, and M. Kawahara, "Characterization of fracture process during ring burst test of FW-FRP composites with damage," *Advanced Composite Materials*, vol. 8, no. 2, pp. 139–151, Jun. 1999.

[9]   E. Brovold and W. Buttlar, "Compact hollow cylinder tensile tester," U.S. Patent 20,010,037,687 A1, Nov. 8, 201.

[10]   P. Rigaud, "Test machine to apply a uniform internal pressure to a tube," U.S. Patent 8,353,217 B2, Jan. 15, 2013.

[11]   E. Fleischlauer, "Pressure fluid ram," U.S. Patent 3044289 A, Jul. 17, 1962.

[12] Alclad Aluminum 6061-T6, T651. (n.d.). MatWeb Material Property Data. [Online]. Available: http://www.matweb.com/search/DataSheet.aspx?MatGUID=3a2e111b27ef4e5d81 3bad6044b3f318. Accessed Apr. 18, 2015.

[13] AK Steel 17–4 PH Precipiation Hardening Stainless Steel, Condition A. (n.d.). MatWeb Material Property Data. [Online]. Available: http://www.matweb.com/search/DataSheet.aspx?MatGUID=20362bbf0a7f45b8ae 59b19a9425239e. Accessed Apr. 18, 2015.

[14] *Standard Test Method for Tensile Properties of Polymer Matrix Composite Materials*, ASTM Standard D 3039/D 3039M, 2008.

[15] *Standard Test Method for Tensile Properties of Platics*, ASTM Standard D638, 2010.

[16] A. Boresi, R. Schmidt, and O. Sidebottom, *Advanced Mechanics of Materials*, 5 ed. New York: Wiley, 1993, p. 459.

INITIAL DISTRIBUTION LIST

1.   Defense Technical Information Center
      Ft. Belvoir, Virginia

2.   Dudley Knox Library
      Naval Postgraduate School
      Monterey, California